Development of an acoustic channel model for a shallow water environment

Propagation model of an underwater acoustic signal

Richard de Jong, David Zwart

Bachelor Thesis

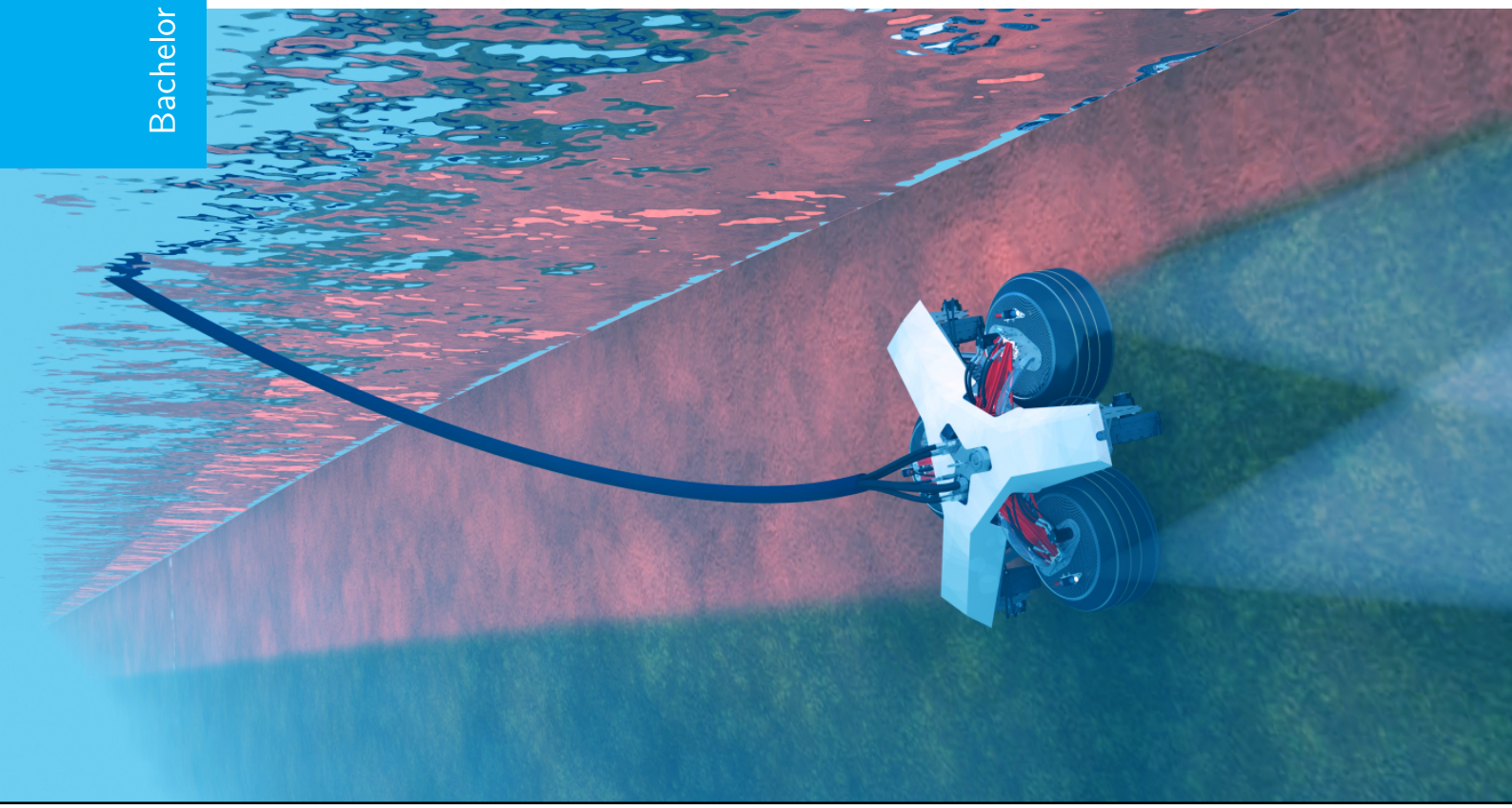

TU Delft Delft University of Technology

BSc Electrical Engineering

Development of an acoustic channel model for a shallow water environment

Propagation model of an underwater acoustic signal

Bachelor Thesis

Richard de Jong 4238575
David Zwart 4224582
BAP H 2016

July 5, 2016

Faculty of Electrical Engineering, Mathematics and Computer Science (EWI)· Delft University of Technology

Fleet Cleaner

The work in this thesis was supported by Fleet Cleaner. Their cooperation is hereby gratefully acknowledged.

Copyright ©
All rights reserved.

Circuits and Systems, TU Delft

Preface

Abstract This thesis shows the successful development of an acoustic channel model to be used for optimisation of localisation. It uses an eigenray approximation, implemented as the image source method to determine a channel impulse response. The image source method however limits the model to environments which can be reduced to cuboid shaped rooms as was the case for the test environment in consideration, the 3mE towing tank of Delft University of Technology. The channel impulse response obtained from the model is validated with an estimated channel impulse response obtained from observed data to have a high similarity.

This thesis is part of the bachelor graduation project of group H. It is a continuation of the work done by Dejan Borota in his MSc Thesis "Design of a position determination system for a ship's hull maintenance robot" [1]. The focus of the project is the creation of a propagation model for an underwater acoustic signal. The subject has been split into three parts: the hardware, the acoustic propagation and the validation. This thesis focusses on the acoustic propagation. This thesis is written by David J. Zwart and Richard J. de Jong.

The thesis on the hardware [2] is written by Joshua Jones and Daan Karman. The thesis on the validation [3] is written by Joris Blom and Costas Kokke.

Acknowledgements The developments regarding the FDTD approach would not have been possible without the help of Dr.ir. Rob Remis, our thanks go out to him.

Table of Contents

Page

1 Introduction **1**

1-1 Scope . . . 1

1-2 Problem Definition . . . 2

1-3 Thesis division . . . 3

2 Requirements **5**

2-1 Model specifications . . . 6

3 Theoretical background **9**

3-1 Sound speed distribution . . . 9

3-1-1 Seasonal variation . . . 10

3-2 Propagation losses . . . 11

3-2-1 Spreading loss . . . 11

3-2-2 Absorption . . . 11

3-2-3 Reflection loss . . . 13

3-2-4 Shear reflection loss and phase shift . . . 15

3-3 Doppler . . . 17

4 Model choice **19**

4-1 Geometric model . . . 19

4-1-1 Ray Tracing . . . 20

4-2 Impulse response estimation . . . 21
4-3 Alternative models . . . 22
4-4 Wave equation models . . . 22
4-4-1 Signal input . . . 23
4-4-2 Finite Difference Time-Domain . . . 23
4-4-3 Pseudo-spectral Time-Domain . . . 24
4-4-4 k-Wave method . . . 24
4-5 Model verdict . . . 25
4-5-1 Ray method . . . 26
4-5-2 k-Wave PSTD . . . 27
4-5-3 Model choice . . . 27

5 Model Implementation **29**
5-1 Image source method . . . 30
5-1-1 Virtual source positions . . . 31
5-1-2 Adapting to harbour environment . . . 32
5-2 Path lengths . . . 32
5-2-1 Path delays . . . 34
5-2-2 Sound speed . . . 34
5-3 Cumulative Reflection coefficient . . . 35
5-3-1 Angles . . . 35
5-3-2 Reflection coefficient . . . 36
5-4 Transfer function . . . 37
5-5 Channel impulse response . . . 40

6 Validation **41**
6-1 Validation of attenuation and dispersion . . . 41
6-1-1 Attenuation coefficient . . . 42
6-1-2 Dispersion & Absorption . . . 42
6-2 Validation through test data . . . 43
6-2-1 Chirp . . . 44
6-2-2 Channel estimation . . . 44
6-2-3 Sound speed estimation from measured data . . . 45
6-2-4 Material properties . . . 46

6-2-5 Comparing channel responses 47
6-3 Adaption to a Fleet Cleaner model 48
6-3-1 Application - model adaptation concepts 49
6-3-2 Shadowing and ray probability analysis 50

7 Conclusion and recommendations **51**
7-1 Conclusion 51
7-2 Limitations of final model 52
7-3 Recommendations 53

A Project Requirements **55**

B Geometry definition **57**

C Complementary model information **59**
C-1 Chen & Millero sound speed model 59
C-2 MAV model parameters 60
C-3 Attenuation and dispersion 61

D Reflections **63**

Bibliography **65**

List of Symbols

$A(f)$	Frequency dependent attenuation
F_s	Sampling frequency
$H(f)$	Transfer function
$H_p(f)$	Path transfer function
R	Radial distance
S	Salinity
T	Temperature
TL	Spreading transmission loss
$Y(j\omega)$	Output frequency response
Δt	Time step
Γ_p	Cumulative reflection coefficient
$\alpha(f)$	Absorption coefficient
$\gamma(\theta)$	Reflection coefficient
λ	Lamé parameter 1
μ	Lamé parameter 2, shear modulus
ρ	Density
τ_p	Path delay
θ_1	Angle of incidence, from medium 1 (water).
θ_2	Angle of transmission, from medium 2 (concrete, steel, etc.).
c	Sound speed
f	Frequency
h	Spatial grid step
k	spreading factor
k_i	Wave number of medium i (normal or shear wave number).
l_p	Path length
pH	Index of acidity
$y(t)$	Output signal
z	Depth

Chapter 1

Introduction

1-1 Scope

Fleet Cleaner develops robots for hull maintenance of ships. The robot cleans and inspects the hull of large ships during loading and unloading in the harbour. The robot attaches itself to the ship magnetically, and moves around using hydraulically powered wheels, with a nominal speed of 1 km/h [1]. The robot operates both above and under water, and will clean and inspect ships during loading and unloading time in the harbour. This means the operational time is limited to the time it takes to unload and load a ship, with the robots diameter of 1.5 meters this takes approximately 8 to 10 hours for ships of around 250 meters in length [1].

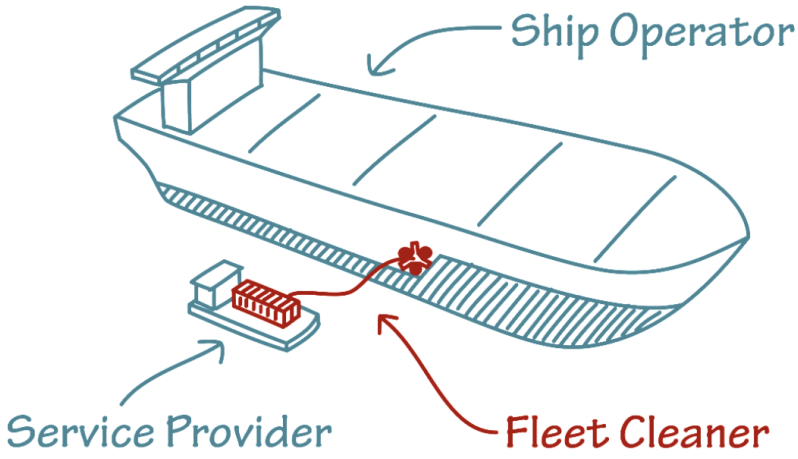

Figure 1-1: The Fleet Cleaner robot operates from a support ship

At this point, the robot is remotely controlled and requires a human operator. Fleet Cleaner's goal is to eliminate the need for a human operator. In order for the robot to operate independently, a positioning system is developed by Fleet Cleaner. Previous work shows that an

acoustic solution is the most optimal approach to this problem. Acoustic wave propagation is more suitable for underwater localisation, since the attenuation of acoustic waves is much less than the attenuation of electromagnetic waves. It has also become clear that direct implementation of available positioning systems does not meet the requirements as set by the Fleet Cleaner company.

The Fleet Cleaner robot will be placed in a shallow water harbour environment on the hull of a ship. Because testing in this environment is not feasible, a test environment is chosen. Because the test environment differs from the operating environment of the Fleet Cleaner robot, a distinction is made between the two environments: the test environment (towing tank) and a real harbour environment.

Fleet Cleaner environment - harbour The Fleet Cleaner robot is placed on the fouled hull of a ship. Concerning acoustic interaction, the ship's hull is thus the nearest reflective object. Secondly, the robot is connected to a support ship (Figure 1-1) with an reflective hull and umbilical (bundle of data and power cables). The geometry and materials are not determined specifically, this information will vary from one ship or harbour to others. Variance in parameters as the speed of sound and inconsistency in the acoustic properties of water complicate this environment. Sensor beacons are placed on the ship to receive the acoustic signal from the robot. These beacons are positioned on translated locations with the known reference location of the ship hull. As acoustic signals, pressure waves under water, travel further the bottom of the harbour and the surface will reflect those waves as well. Besides the changes in geometry compared to the towing tank there will be a lot more noise as well. Ambient noise, noise from human interaction (other ships/ machinery), but also some unexpected reflections might occur due to the uncertainty in the environment.

Test environment - towing tank As test environment the towing tank at the faculty of 3mE at the Technical University of Delft is used. This towing tank has dimensions (length: 142.00 m, width: 4.22m, depth: 2.50m). Compared to the Fleet Cleaner environment, the towing tank is relatively small in width and depth as shown in Figure 1-2. The towing tank has reflective boundaries on all sides. In the test environment geometric data can be measured precisely, but in real application this is not feasible for all objects with acoustic interaction. The precisely known geometry of the towing tank is the primary advantage of this test environment. The disadvantage of the testing tank shows in the amount of reflections and the low attenuation of nearby echo's, which could make distinguishing reflections more difficult.

1-2 Problem Definition

The goal of the project is to derive a data model for the shallow water acoustic channel containing multi-path propagation, using the available acoustic positioning equipment. The model should be based on appropriate theoretic framework from literature, with experimental validation.

Previous tests showed that the positioning system was either too inaccurate or sensitive for too many variables. Although some of the problems have been mapped or qualified, some

Figure 1-2: Part of the towing tank in Delft

unknowns prohibit the system from working as required and need quantification. The main problem then summarises as follows: *The acoustic patterns transmitted and received by hydro-acoustic transducers*[1] *can't yet be separated and coupled to the channel history and discrete acoustic events in the channel.*

The focal point of this project is therefore the creation of an acoustic model of signal propagation through a shallow water harbour environment to be used for optimisation of localisation.

The project coupled to this thesis involves more than the acoustic model, references are made to previous and currently developed work concerning the modelling of the used hardware components, the analysis of the input signal and the validation tools for qualifying the model with observed data.

1-3 Thesis division

Chapter 2 describes requirements for the model considering the Fleet Cleaner environment. Chapter 3 sets a basis of theory supporting the calculations and approximations for the geometric ray-approximation model chosen in Chapter 4, which meets the set requirements. Chapter 5 uses the theoretical basis and discusses the model algorithms and implementation. In Chapter 6 validation of the model is done using observed data, showing the simulation resulted in successful prediction of the test data. Chapter 7 concludes the results and a recommendation is made for further development of the acoustic channel model.

[1] An acoustic microphone for use in water.

Chapter 2

Requirements

This Chapter contains the programme of requirements. The requirements mentioned in this Chapter are the functional requirements relevant for the acoustic channel model. The requirements for the entire project, the propagation model of an underwater acoustic signal, can be found in Appendix A. The requirements set are partly based on findings in literature. The results of the studied literature are given in Chapter 3.

One of the key components for the acoustic model is the fact it will be used for optimisation of localisation, hence it should fit with the primary specifications used for localisation. The requirements relevant for the acoustic propagation model are given below. For convenience the numbering is the same as in the Appendix.

R1 All models, the hardware models and the acoustic propagation model, must be compatible to the validation scheme and musst be combined into one simulation model.
R2 All models must be able to aid in localisation when combined.
R3 Time of Flight estimates must have an accuracy of 70 microseconds or less[1].
R4 The acoustic model must determine a channel impulse response
R7 Hardware model must only model the specific hardware made available by Fleet Cleaner.
R8 Acoustic model must have a simulation time of less than 30 seconds.
R9 Acoustic model must be able to model reflective paths.
R10 Acoustic model must model the geometry of the towing tank[2].
R11 Acoustic model must take material properties into account for each boundary (surface and walls).
R12 Acoustic model must model in 3D.
R13 Acoustic model must take arbitrary source and receiver positions in the towing tank into account.

Besides the acoustic propagation model, a model for the used hardware is made [2]. The models must be compatible to combine them into one simulation model, although this thesis focuses on the acoustic propagation it must be compatible with the used hardware.

[1] 70 microseconds corresponds to a 10 centimetre accuracy approximately.
[2] The large towing tank of 3mE.

The goal of Fleet Cleaner is to make a positioning system for the robot, the model must therefore be able to aid in this localisation when combined. Localisation techniques often use channel estimation techniques to determine the time of flights of the signals going through the channel. The time of flight information is used to estimate the position. The model must therefore be able to determine a channel impulse response to aid in this localisation. The accuracy of $70\mu s$ results in an approximate resolution of $10cm$ and is set as a minimum accuracy. The time of flight is proportional to the distance and sound speed, this means the sound speed and the distance need to be known precisely.

Some models found were computationally intensive, as requirement a simulation time of less than 30 seconds is set to prevent the model of becoming too complex.

A key component of the test environment and the Fleet Cleaner environment are the many reflections occurring and interfering with the received signal. A model describing these environments should thus be able to take these paths into account, preferably a variable amount of reflections can be determined to investigate the influence of the different reflections on the received signal. Validation in a real Fleet Cleaner environment is infeasible, therefore a model will be created which models the towing tank and thus the geometry of the towing tank needs to be included. Because the test environment and the Fleet Cleaner environment are both 3 dimensional spaces, the model must be able to model the environments in 3D. A 2 dimensional model will not be able to aid in localisation as a 3 dimensional model can do. The receiver and transmitter might be placed at any arbitrary position in the towing tank and thus the model must be able to determine a channel impulse response for any arbitrary position in the towing tank.

2-1 Model specifications

Based on the requirements and the theory/model possibilities, Table 2-1 structures the acoustic model by priority and expected impact.

Must have	**Should have**	**Could have**
Uniform (flat) geometry	Shadowing zones	Beam scattering
Reflections	Shear waves	Doppler shift
Reflection coefficients	Phase shift at air boundary	Noise source addition
Variable amount of reflections	Phase shift (other surfaces)	Non-uniform geometry
Absorption model	Sound speed estimation	
Channel impulse response	(variable) Material properties	
Path delays	Directivity	

Table 2-1: Model aspects, prioritised.

The model must at least include the components mentioned in the *must have* column. The geometry of the environment is an important aspect for the acoustic propagation, hence the model must include a (simplified) description of the geometry, including the transmitter and receiver location. A key component of the shallow water environment is the great amount of reflections occurring along the channel, therefore they must be included in the model.

Every reflection is accompanied with a loss in signal strength, which is quantised by the reflection coefficient. Only some specific type of reflection results in shear waves, this will be

taken into account if deemed necessary. To determine the influence of the different reflections on the received signal a variable amount of reflections will be taken into account. For propagation over longer distances the frequency dependent attenuation becomes relevant and thus this will be included in the model.

Shadowing is the phenomenon of acoustic signals becoming trapped in a cavity or when the line of sight is blocked by a big object. This is only implemented when such cavities or obstructions are expected in the testing environment.
The model must be able to determine the channel impulse response for a given transmitter-receiver location, this includes a determination of the path delays.

The time of flight is associated with the path delay and requires a precise sound speed to meet the set requirement of estimating the time of flights within $70\mu s$. A first sound speed will be determined based on sound speed models found in literature. An effort will be done to estimate a more precise sound speed based on the measured data.

A more realistic harbour environment will not only have perfect flat smooth surfaces but curving boundaries or even other objects in place, causing the waves to scatter when they interact with a wall or other object. To investigate the propagation of the signal through such a channel a non-uniform description could be included in the model. Because the effect of different localisation techniques can already be tested with a more simplified model this is of lesser importance. The influence of Doppler shift seemed to be negligible and is therefore placed in the could have column.

Chapter 3

Theoretical background

This chapter gives some theoretical background on acoustic wave propagation which will be used in elaborating different models/methods in Chapter 4. This theory supports the argumentation on how the model is implemented in Chapter 5 and validated in Chapter 6.

The following variables have to be considered for a model describing the propagation of acoustic wave signals in an underwater environment, adapted from [1]:

- Natural non-ideal properties of water
- Signal spreading
- Absorption
- Noise
- Multi-path propagation

Acoustic waves oscillate in longitudinal direction, which is the propagation direction. At a boundary the wave is split into a longitudinal reflected wave with a decreased amplitude, a transversal refracted wave and a longitudinal refracted wave. Some energy of the wave is thus absorbed in the reflective medium. The second energy absorption is apparent throughout the propagative medium. Water absorbs more wave energy depending on the frequency and distance travelled by the wave. This chapter gives more detail on how acoustic absorption occurs and how these effects are modelled.

3-1 Sound speed distribution

Sound refraction in the water is a consequence of the spatial variation of the sound speed c. This speed depends on the temperature, salinity and pressure of water which depend on the depth and location. Many empirical formula's have been developed over the years for calculating sound speed using the values for water temperature, salinity and pressure/depth. The Medwin formula is an example of such empirical approaches. This expression [4] for the sound speed is Eq. (3-1):

$$c = 1449.2 + 4.6T - 0.055T^2 + 0.00029T^3 + (1.34 - 0.01T)(S - 35) + 0.016z \qquad (3\text{-}1)$$

Where T is the temperature (in degrees Celsius), S the salinity (in parts per thousand) and z the depth (in meters). The Medwin model is meant for rapid computation. More computationally-intensive models are available to determine an accurate sound speed [5, 6]. The Chen & Millero model for sound speed in water is a model adopted by UNESCO in 1983. This empirical model is fitted with more parameters than the Medwin model and is thus more precise for the same range of temperature, salinity and depth/pressure. The models are both meant for a depth range of 0m - 1000m and can be converted to tap water, basin water, brackish water and sea water. Both models show most variation for temperature. Salinity and depth do have an effect, but this effect is less noticable [6]. The Chen & Millero model is more precise because of it's higher order of parameters and it is approved by UNESCO, therefore this model is used from now on. It can be found in Appendix C-1 in MATLAB code.

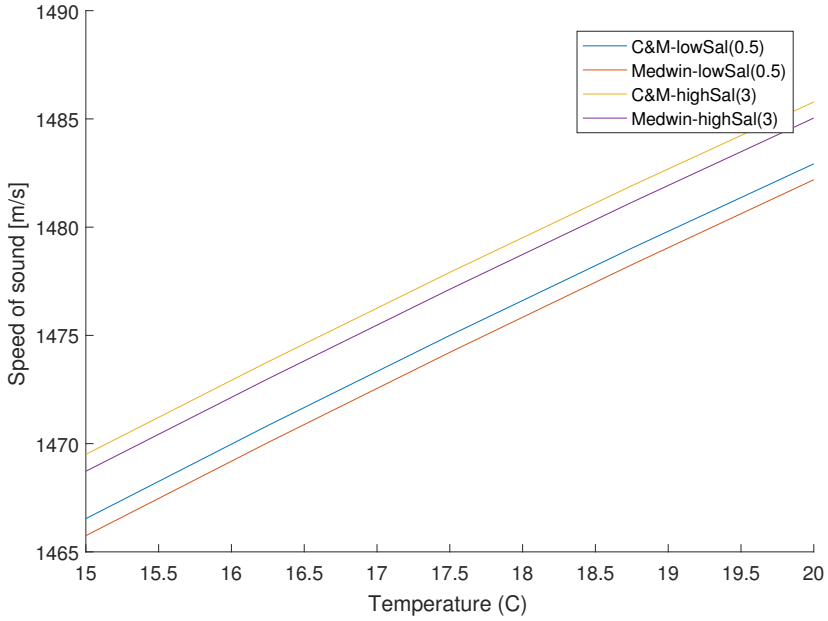

Figure 3-1: Multiple sound speed curves for Medwin and Chen & Millero model for salinity of 0.5 and 3.0 ppt at 0m depth.

Figure 3-1 shows quite some variation over temperature for both models. It also shows that the models are less variant for different salinities.
The UNESCO model shows a constant 0.48 m/s deviation for between 0m depth and 30m depth over this temperature range. The Medwin shows a near linear deviation from 0.48 m/s deviation to 0.489 m/s for 0m depth to 30m depth over these temperatures. Both deviations of sound speed for change in depth are small enough to be considered negligible.

3-1-1 Seasonal variation

In shallow water near the surface, ~30 meters, sound speed is nearly constant [7, 8]. For greater depths the sound speed changes depending on the season. A typical winter sound

speed profile shows a constant sound speed (± 1500 m/s) for the first 100 meters. A typical summer sound speed profile shows a larger sound speed (± 1530 m/s) for the first 30 meters and a drop in the sound speed after the first 30 meters. Beyond 40 meters the sound speed profiles overlap. This is the result of the top layer of the water being heated in the summer. To estimate the effect of seasonal variation only temperature is required, since depth variation is negligible. The temperature of the test environment and the Fleet Cleaner environment can be estimated or measured. Therefore the sound speed in water can be determined and assumed invariant for depths less than 30 meters.

3-2 Propagation losses

Propagation losses are the cause of the decay in signal power between the beacon transducer (input) and the receiver transducer (output). The propagation losses can be divided in three groups: spreading loss, absorption losses and reflections losses.

3-2-1 Spreading loss

An acoustic wave emitted from a point source will spread the transmitted acoustic energy over a spherical surface increasing in radius. The spreading loss, or transmission loss, is expressed by the following equation [9]:

$$\mathrm{TL}_{spreading} = 20log(R) \tag{3-2}$$

with TL the transmission loss in dB and R the (radial) distance from the source (in meters). This transmission loss refers to the acoustic intensity which decreases as $1/R^2$ while the pressure decreases as $1/R$ [9].

3-2-2 Absorption

Not only spreading causes a decay in signal strength. Part of the energy of the acoustic wave is absorbed, attenuated, by the lossy medium which the pressure wave travels through. Therefore Equation (3-2) is adapted to fit both spreading loss and absorption loss:

$$\mathrm{TL} = 20log(R) + \alpha(f) \cdot R \tag{3-3}$$

With TL the transmission loss in dB, R the radial distance (in meters) and α a frequency dependent absorption coefficient in dB/m. Different equations/models can be used to determine this absorption coefficient [10]. A list of the absorption models found is given below.

- Thorp
- Francois-Garrison (F&G)
- Fisher and Simmons (F&S)
- Ainslie and McColm (A&M)
- Moll, Ainslie and van Vossen (MAV)

Thorp is only valid for frequencies under 50 kHz [9] and is therefore not applicable. Fisher and Simmons [11] and Ainslie and McColm [12] are only valid if the water has a fixed salinity of 35 ppt (parts per thousand), this is a strict limitation and far from reality in case fresh water is used, as is the case in the test setup.

F&G is valid for a salinity between 30 and 35 ppt where MAV is valid for salinity between 8 and 40 ppt. MAV is valid for a temperature of $-1.75°C$ to $22°C$ and a frequency range between $0.16kHz$ and $650kHz$. The MAV model is in accordance with most of the test setup variables and is thus adapted. The specifications of the MAV model are shown in Table 3-1. This attenuation model is not ideal for a fresh shallow water environment but it corresponds the most with the test environment. The model is based on empirical data and uses data from measurements in the ranges given in Table 3-1.

Table 3-1: MAV model specifications [13]

variable	Range	Units
f	[0.16, 650]	kHz
pH	[7.69, 8.18]	
S	[8, 40.5]	g/kg
T	[-1.75, 22]	$°C$
z	[0.013, 3.35]	km

This attenuation model requires a frequency (kHz), salinity in (g/kg), temperature (°C), depth (km) and a pH value of the water as input. The MAV model is described by the following equation [13]:

$$\alpha_{dB} = A_1 * P_1 * \frac{f_1 * f^2}{f_1^2 + f^2} + A_2 * P_2 * \frac{f_2 * f^2}{f_2^2 + f^2} + A_3 * P_3 * f^2 \tag{3-4}$$

This equation is composed of different terms, corresponding to the dissipation contributions of boric acid (term 1), magnesium sulphate (term 2), and pure water (term 3). Using the set of parameters in Appendix C-2

The temperature in the test environment was measured at $15°C$. The salinity of fresh water and the pH value were determined from literature to be $S = 0.5$ ppt and $pH = 7$. The MAV model is accurate from a depth of 13 meters while the depth of the test environment is just 2.5 meters. To stay within the limits of the absorption model the depth was set at 13 meters, the pH at 7.69 and the salinity at 8 ppt. The model output is shown in Figure 3-2a. The attenuation is calculated for the frequencies ranging from 0 kHz to 250 kHz because the sample rate of the hardware used is $Fs = 500kHz$. The Nyquist frequency [14] tell us the max frequency in the sampled signal can be $Fs/2$ and thus there is no need to determine the attenuation for higher frequencies.

Because the absorption model gives α in dB/km and the used model, Equation 4-3 (described in the Chapter 4), requires α in gain/m this was transformed according to Equation 3-5.

$$\alpha(f) = 10^{\alpha_{dB}/10000} \tag{3-5}$$

In Figure 3-2b the absorption model for the used settings is shown, the graph shows the attenuation as gain per meter for the corresponding frequencies. The effect of frequency

attenuation becomes significant for greater distances, over 50 meters the attenuation for 170 kHz is $1.0044^{50} = 1.2455$, meaning an additional decrease in signal power.

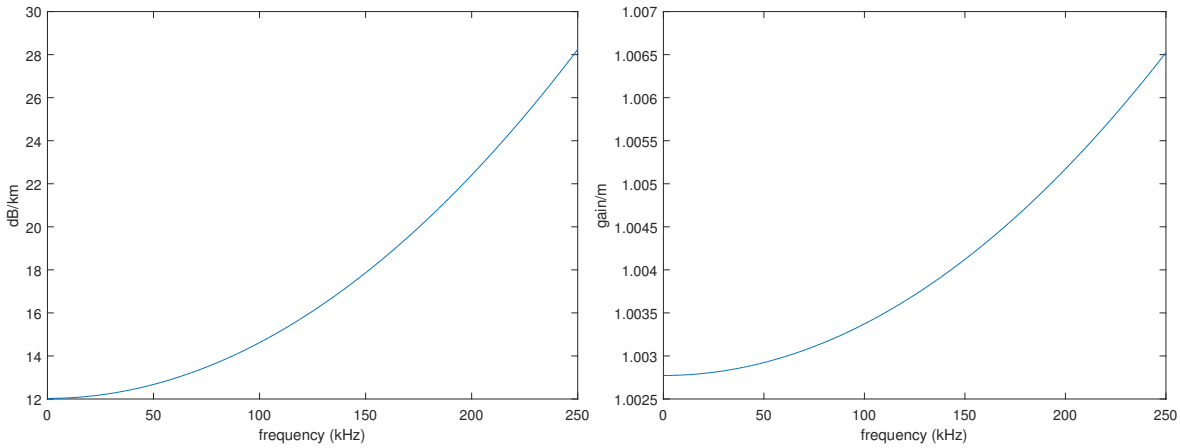

(a) The attenuation in dB per kilometer **(b)** The attenuation per meter

Figure 3-2: Attenuation. S = 8 ppt, pH = 7.69, T = 15°C and z = 13 meter

3-2-3 Reflection loss

In case a acoustic plane wave is incident upon an interface between two different media[1] part of the wave is reflected and another part is transmitted into the target medium. The reflected wave will propagate in a direction symmetrical to the incident wave relative to a normal vector on the surface. This is also called "Specular Refraction" [9]. The transmitted wave obeys Snell-Descartes law

$$\frac{sin(\theta_1)}{c_1} = \frac{sin(\theta_2)}{c_2} \tag{3-6}$$

where c_1 is the sound speed in the medium the wave is travelling through, θ_1 is the angle of the incoming wave relative to the normal of the surface, θ_2 is the angle of the transmitted wave relative to the normal to the interface and c_2 is the sound speed in the reflective medium. Equation 3-6 can be solved for θ_2 as follows:

$$\theta_2 = sin^{-1}(\frac{c_2 \cdot sin(\theta_1)}{c_1}) \tag{3-7}$$

Equation 3-7 turns complex for $\theta_1 > 45$ degrees or $sin(\theta_2) > 1$, because $sin^{-1}(x)$ for $x > 1$ becomes complex. This angle represents the critical angle. The critical angle θ_c, the limit of θ_1, is then defined as follows:

$$\theta_c = sin^{-1}(\frac{c_1}{c_2}) \tag{3-8}$$

The amplitude of the transmitted and reflected wave are given by the reflection coefficient γ and the transmission coefficient T. The critical angle separates total reflection ($|\gamma| = 1$) and reduced reflection ($|\gamma| < 1$) which is shown in Figure 3-3. It is clear that no transmission or

[1]Medium 1 is defined as the medium from which the plane wave arrives towards the boundary. Medium 2 is the medium on the other side of the boundary.

energy loss occurs for an ideal reflection with an angle of incidence greater than the critical angle. The reflection and transmission coefficient are determined as [7, 9]:

$$\gamma(\theta_1) = \frac{\rho_2 c_2 cos(\theta_1) - \rho_1 c_1 cos(\theta_2)}{\rho_2 c_2 cos(\theta_1) + \rho_1 c_2 cos(\theta_2)} \tag{3-9}$$

$$T(\theta_1) = 1 + \gamma(\theta_1) \tag{3-10}$$

With ρ_1 and ρ_2 as the density [kg/m^3], c_1 and c_2 the sound speed [m/s] of medium 1 and 2.

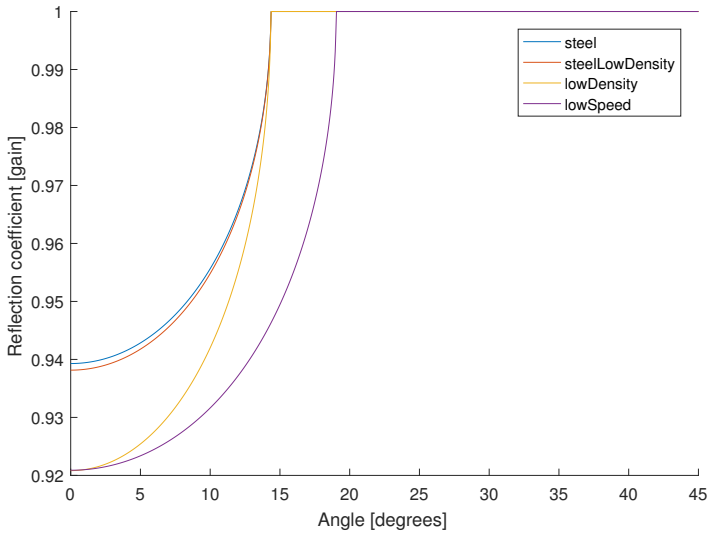

Figure 3-3: Reflection coefficient ($|\gamma|$) for θ_1 with medium 2: steel, lower-density steel, much lower density medium and lower sound-speed medium. Medium 1 is water.

Material	**Sound speed** c_2	**Density** ρ_2	**Critical angle** θ_c
Steel	5920	7900	14.79
Low density steel	5920	7750	14.79
Low density material	5920	6000	14.79
Low sound speed material	4500	7900	19.20
Water	1480	998	-

Table 3-2: Example medium parameters for Figure 3-3

Figure 3-3 shows how different materials relate to each other in reflection coefficient. The parameters for these graphs are presented in Table 3-2. Increasing the density causes an increase in reflection coefficient. Decreasing the sound speed for the secondary medium (into which transmitted waves propagate) increases the critical angle and therefore the angle at which the reflection angle becomes complex.

Not only longitudinal or compressional waves result from reflection upon an elastic medium[2]. Shear waves are created in the elastic medium, which affects the reflection coefficient as is explained in the next Section.

[2] A medium which is highly resistant to compression and shearing. A medium which restores to it's original shape after compression.

3-2-4 Shear reflection loss and phase shift

Upon reflection on elastic, dense materials longitudinal waves are reflected and transmitted. Acoustic waves do not only oscillate in longitudinal direction in elastic materials, but also in transverse direction. Transverse waves can develop at the boundary reflection caused by longitudinal waves, which means more energy is absorbed. Transverse waves are therefore defined as shear waves in this section. Equation 3-9 is not valid for this type of absorption. Equation 3-11 includes shear waves in the reflection coefficient.

$$\gamma = \frac{B-1}{B+1} \tag{3-11}$$

With B defined as follows:

$$B = \frac{\rho_2}{\rho_1}\frac{1}{k_S^4}\frac{k_{z1}}{k_{z2}} \cdot [(k_{zS}^2 - k_{x1}^2)^2 + 4k_{x1}^2 k_{zS} k_{z2}] \tag{3-12}$$

Where wave number k is defined for medium 1 and medium 2 and ρ_1 and ρ_2 the corresponding densities. This equation is defined with wave number for medium 1, medium 2 and the shear wave number for medium 2. Medium 1 is assumed to be water throughout this thesis. Medium 2 is assumed to be either elastic, solid and dense materials or air. Note that, since medium 1 is water and thus non-elastic, no shear wave number is defined for medium 1.
The wave number is defined as follows:

$$k = \frac{2\pi f}{c} \tag{3-13}$$

Where f is frequency. This formula suggest that the reflection coefficient becomes frequency dependent with including shear waves, but this is not the case. f disappears from equation 3-12 when all wave numbers are inserted.
The definition of the wave number allows defining the wave numbers k_S, k_{z1}, k_{z2}, k_{zS} and k_{x1}. k_i is the medium wave-number for medium i (1 or 2) and $[k_{xi},\ k_{zi}]$ orthogonal components compared to the normal vector of the boundary defined on the (x,y)-plane. $\hat{\mathbf{x}}$ is defined as the normal component and $\hat{\mathbf{z}}$ the tangential component.

$$[k_{xi}, k_{zi}] : \begin{cases} k_i \cdot sin(\theta_i) & i = 1 \\ k_i \cdot cos(\theta_i) & i = 1, 2, S \end{cases} \tag{3-14}$$

Note that the shear wave speed[3] needs to be found in order to compute the reflection coefficient in case of the both longitudinal and transversal wave reflection.
The wave-speed c_2 and shear wave-speed c_S are found through the two Lamé coefficients μ and λ:

$$[c_i, c_S] : \begin{cases} c_2 = \sqrt{\frac{\lambda+2\mu}{\rho_2}} \\ c_S = \sqrt{\frac{\mu}{\rho_2}} \end{cases} \tag{3-15}$$

Where λ is Lamé's parameter 1, μ is the shear modulus, Lamé's parameter 2 and ρ the medium density.

[3]Shear wave speed is the sound speed for shear waves travelling through elastic media.

Note that since no shear wave-speed is defined for medium 1, only a solid as medium 2 can have a shear wave-speed parameter. Also note that in Section 3-1 we defined the wave-speed through an approximated model with fluid parameters. Therefore only the wave-speed in medium 2 is defined in Equation 3-15. The result is that λ will not be computed as it is not used.

The reflection coefficient for shear wave speed results in a new critical angle θ_{csh}. When the angle of incidence θ_1 is larger than this angle, the boundary will show pure reflection and only phase shift. θ_{csh} is derived from Equation 3-8 (Snell's law):

$$\theta_{csh} = sin^{-1}(\frac{c_S}{c_2}) \tag{3-16}$$

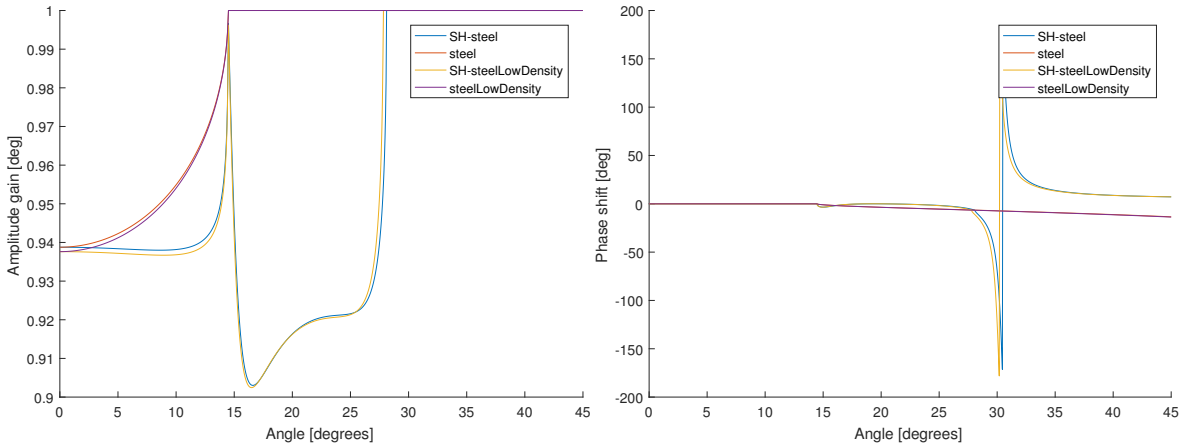

(a) Magnitude of reflection coefficient ($|\gamma|$). **(b)** Phase of reflection coefficient ($\angle\gamma$).

Figure 3-4: Magnitude and phase plot for media as defined in Table 3-3 including shear and normal reflection.

Figure 3-4 shows the effect of including the shear wave approximation. The reflection coefficient is greatly affected in the range $\theta_c < \theta_1 < \theta_{csh}$. The phase response shows change, near the critical angle θ_c. Concluding both the shear wave reflection and normal wave reflection should be included to estimate this loss. The phase shift of the signal occurs at the shear critical angle when the reflection amplitude becomes unity. It will add phase shift to only higher angle reflections.

Material	c_2	c_{shear}	ρ_2	μ_2	θ_c	θ_{csh}
Steel	5920	3142	7900	$78*10^9$	14.5	28.1
Low density steel	5920	3172	7750	$78*10^9$	14.5	27.8

Table 3-3: Example medium parameters for Figure 3-4 with shear waves.

Equation 3-11 is used in Chapter 5, where a more realistic approach to the parameters in Table 3-3 for actual media are estimated.

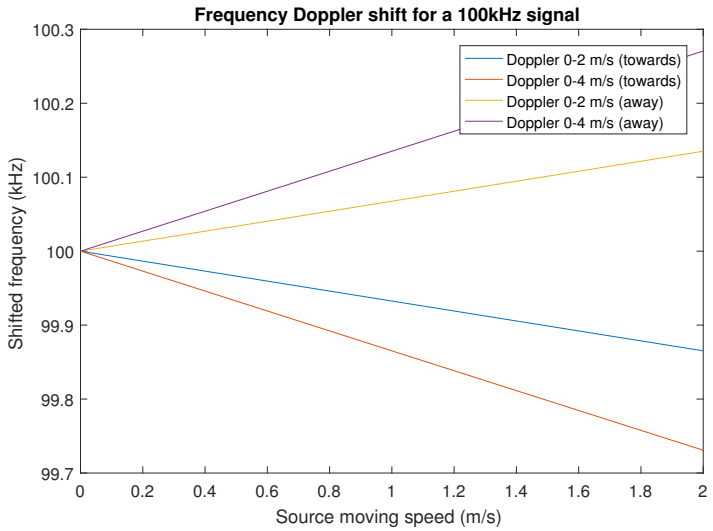

Figure 3-5: Doppler shift of 100kHz signal for multiple source moving speeds.

3-3 Doppler

The Doppler effect defines stretching and folding of frequencies in the time and distance domain. The frequency content of the signal become dependent on the speed of the source and receiver object. Since it is a non-linear operation, there is no direct mathematical counterpart of the Doppler effect on the whole frequency spectrum.

The influence of the Doppler effect can be estimated by calculating the Doppler shift for a certain frequency and speed in the time domain by approximating the signal with one frequency. This gives an estimation as to how much the frequency content is altered when plotted for varying moving speed or frequency.

The following formula defines the Doppler shift:

$$f_{shift} = \begin{cases} \frac{c}{c-c_s} \cdot f_{source} & \text{for moving away} \\ \frac{c}{c+c_s} \cdot f_{source} & \text{for approaching} \end{cases} \tag{3-17}$$

Figure 3-5 shows that the Doppler shift has minimal effect on the resulting frequency for constant source velocity. Therefore the static Doppler effect is assumed to be negligible. It remains to be quantified how much accelerated motion distorts the channel. It is expected to have major impact on the received signal.

Chapter 4

Model choice

The models/methods used are discussed in Section 4-1 (Geometric model) and in Section 4-2 (Impulse response estimation). Alternative models are discussed in 4-3 and the finite-difference time domain model (FDTD model) is discussed in Section 4-4.

The acoustic channel model assumes an interface between a source/receiver and the channel. The source converts the applied voltage to a pressure and the receiver converts the pressure to a voltage. The channel models interest is thus the pressure relation between the transmitter and receiver. Throughout this chapter the assumption is made that the source and receiver(s) are point elements. Although the used hydrophones are spherical shaped objects with a diameter of $2cm$ [2], the required localisation precision of at least $10cm$ exceeds the size of the hydrophone and transducer by far. Therefore, the assumption to estimate these elements as point sources is based on the fact that taking a spherical approximation of a real acoustic interface will not necessarily yield a higher localisation precision.
Every source has a slightly different output gain for a range of observed angles. However, this directivity will be assumed uniform for all angles since only for a very limited range of output angles there exists a low output gain. This is shown in the directivity plots of the acoustic transducer-models [2]. The advantage of such an approach is that the radiated signal becomes a spherical pressure-wavefront with a uniform distribution of radiated energy for all directions. The eigenray approach in section 4-1 takes advantage of this phenomenon by approximating this wavefront as infinite amount of rays.
The FDTD-approach in Section 4-4 does assume a point source, but it does not approximate the uniform wavefronts as rays.

4-1 Geometric model

In an acoustic channel propagation occurs over multiple paths. In water the multipath formation is governed by two effects: sound reflection at the surface, bottom and any objects and sound refraction in the water.

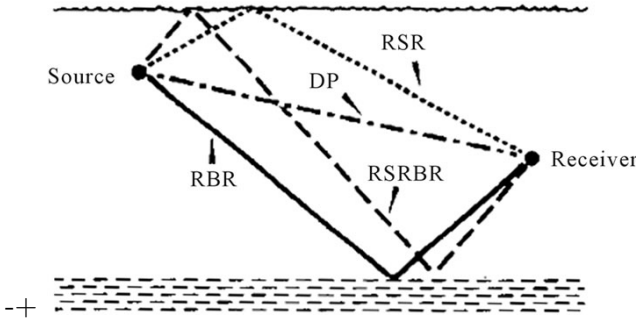

Figure 4-1: 4 eigenrays: Direct Path (DP) - Refracted Bottom Reflected (RBR) - Refracted Surface Reflected (RSR) - Refracted Surface Reflected Bottom Reflected (RSRBR) [5]

The shallow water environment can be modelled as a volume of water with a bottom and a surface (and possibly other boundaries on the sides). By connecting direct and reflected paths from source to receiver patterns arise, these unique connections are called eigenrays. In Figure 4-1 four eigenrays are shown for a shallow water environment. These eigenrays are the paths connecting the source and the receiver. There are more possible eigenrays connecting the source and the receiver, infinitely many eigenrays can be defined, but higher order reflective rays are attenuated by dispersion loss and an increasing number of reflection losses. Modelling the spherical wavefront as a ray is a valid approximation for high frequencies ($> 500Hz$) [4, 5]. Because the signals transmitted are well above this frequency this is a valid approximation. The test environment used can be modelled as a rectangular box. Therefore a geometric approach is feasible. The path lengths and angles can be determined from the geometry of the environment.

4-1-1 Ray Tracing

Due to the spatial sound speed distribution rays as illustrated in Figure 4-1 might become curving lines, as discussed in Section 3-1. Due to the different sound speeds the ray of sound bends toward the region of lower propagation speed - obeying Snell's law with infinitesimally small sound speed layers. The propagation distance from the rays changes and the path dependent attenuation changes compared to the bare geometric model. An algorithm implementing ray tracing requires a sound speed distribution as input. The algorithm can be considered as having three stages [15]:

- The initial ray tracing using a large number of rays to map out the entire sound field.
- Sorting and interpolation to determine the trajectories and the ray history of the eigenrays connecting the source to the receivers.
- Synthesis of the acoustic field in frequency domain by coherently adding the contributions of the eigenrays, and calculation of the full-waveform time responses by Fourier transformations.

Instead of the last step described above, once can also use the impulse response estimation method described in Section 4-2. The sound speed is expected to be fairly constant in the op-

erating region as explained in Section 3-1, especially in case of the 3me towing tank, therefore the bending of rays is expected to be negligible and thus ray tracing is not implemented.

4-2 Impulse response estimation

In an underwater acoustic channel propagation occurs over multiple paths. The gain of a single path can be denoted by [16]

$$h_p = \frac{\Gamma_p}{\sqrt{A_p}} \tag{4-1}$$

where h_p is the gain of the $p-th$ path, Γ_p is the cumulative reflection coefficient and A_p the propagation loss along the p-th path. Although this does not take into account the frequency dependent attenuation. To account for the frequency dependency a single path can be modelled as a low-pass filter whose transfer function can be described by:

$$H_p(f) = \frac{\Gamma_p}{\sqrt{A(l_p, f)}} \tag{4-2}$$

where $H_p(f)$ is the transfer function [17, 18]. The cumulative reflection coefficient Γ_p is the product of all the individual, angle dependent, reflection coefficients a path (ray) interacts with. The water surface can be modelled with a reflection coefficient $\gamma_s = -1$ [9], while the bottom and walls absorb part of the signal as discussed in Section 3-2-3.

The attenuation of a single path can be represented as a gain (a factor between 0 and 1) and is described by [17]

$$A(l_p, f) = A_0 \cdot l_p^k \cdot \alpha(f)^{l_p} \tag{4-3}$$

where k is the spreading factor between 1 or 2 (for respectively cylindrical and spherical spreading), l_p the path length in meters, f the frequency in Hertz, A_0 a constant scaling factor and $\alpha(f)$ the absolute attenuation per meter. The path length l_p can be extracted from the geometry of the environment. Equation 4-3 looks similar to Equation 3-3. Taking the logarithm of 4-3, setting $k = 2$ (spherical spreading) and $A_0 = 1$ (to avoid scaling the attenuation), the following results:

$$10\log(A(l_p, f)) = 20\log(l_p) + 10\log(\alpha(f)) \cdot l \tag{4-4}$$

the difference between the equations is the unit of the attenuation.

Each path contributes to the overall impulse response. All the paths can be summed:

$$h(t) = \sum_p h_p(t - \tau_p) \tag{4-5}$$

where $h(t)$ is the channel response and $h_p(t)$, the impulse response of a single path, is the inverse Fourier transform of $H_p(f)$ and

$$\tau_p = l_p/c \tag{4-6}$$

is the propagation delay associated with the p-th path. With c the speed of sound (m/s). The time delay corresponds to a phase shift in the frequency domain [16]

$$H(f) = \sum_p H_p(f) e^{-j2\pi f \tau_p} \tag{4-7}$$

with $H(f)$ the transfer function of the entire channel. The desired output $y(t)$ can be obtained by convolving the impulse response with the input $u(t)$ [14]:

$$y(t) = h(t) * u(t) \tag{4-8}$$

where $y(t)$ is the output signal for a given input $u(t)$. The same result can be obtained by doing a multiplication in the frequency domain.

$$Y(j\omega) = H(j\omega)U(j\omega) \tag{4-9}$$

The transfer function $H(j\omega)$ can be obtained by taking the Fourier transform of $h(t)$. Equations (4-5)(4-7)(4-8)(4-9) apply in general to methods which determine an impulse response of the channel. The impulse response estimation method as described above allows to calculate an impulse response of the acoustic channel independent from the input and will be used combined with the geometric approach described in 4-1.

4-3 Alternative models

Besides the ray theory as discussed in Section 4-1 alternative models exist. Some model types mentioned in literature are range-independent (normal mode, multipath expansion and fast field). Ray theory is range dependent[1]. Since the model specifications in Section 2-1 state that both reflections and range-dependent absorption must be included, normal mode, multipath expansion and the fast-field approximation are not suitable and rejected as solutions.
The next section explains the FDTD and PSTD methods (and implementations of these models), which are based on range-dependent models.

4-4 Wave equation models

This section discusses the Finite-Difference Time Domain (FDTD), Pseudo-Spectral Time Domain method (PSTD) and kspace PSTD method. These methods approach the wave equation by dividing the domain into a grid for both time and position and applying approximations to this division. Every grid cell is dependent on the neighbour cells as shown in Figure 4-2a and 4-2b.

[1]Literature defines range-dependency as follows: A model is range-dependent when the channel response depends on the absorption caused by distance or angle of acoustic pressure waves on receivers. Both range-dependent and -independent models can be depth dependent. [4, 5]

4-4-1 Signal input

Real and continuous signals must be sampled and discretized in order to function as input. The signal is filtered before it is put into the model. Finite time signals can be approached with wideband-limited signal models to calculate the propagation of the transient response in the channel [5] (spatial propagation). This effectively sets the initial conditions for an approximation for an acoustic source. Previous discussed models - ray tracing and impulse response estimation - are frequency domain models and do not depend on a spatial grid division. Therefore those models do not require initial conditions for the source.

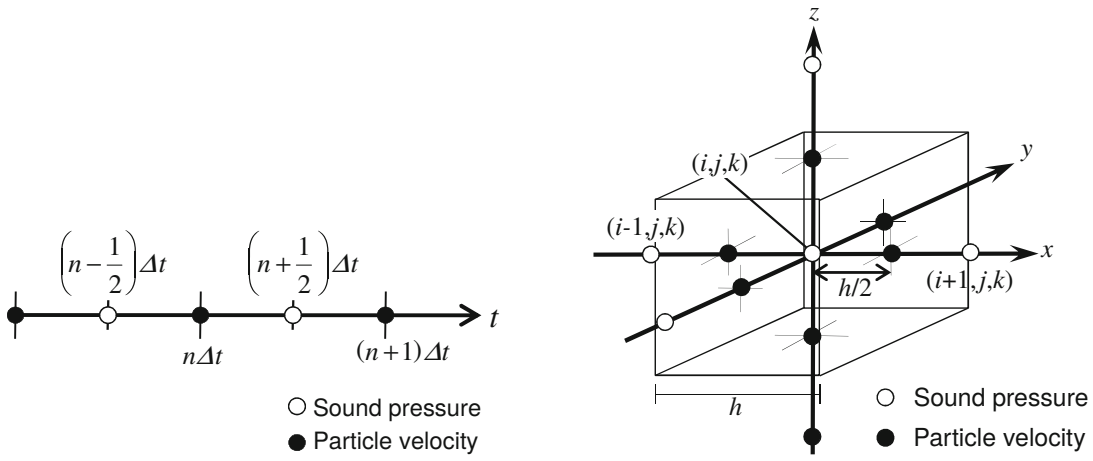

(a) 1D cell. Δt: time-step size, n: spatial grid size

(b) 3D cell. $[i, j, k]$: location vector

Figure 4-2: FDTD 2D and 3D - adapted from [19].

Figure 4-2a and 4-2b visualizes how a FDTD cell and it's boundary values are defined for 1D and 3D.

4-4-2 Finite Difference Time-Domain

Simulation of the wave equation approximation is in essence a multi-dimensional problem. An ill guess would be to model a pressure/speed dependent vector field in a 2D-plane, because pressure waves spread out radially in a 3D-field. Therefore simulating acoustic waves in a 2D-plane, one assumes all energy propagated in the third dimension is never reflected - it disappears in another dimension and can not interfere with the 2D model.

Literature shows that the FDTD method requires approximations for ideally matched boundary conditions [19]. These boundary conditions can be approximated by a perfect matched layer - an absorbing boundary condition (PML; ABC) [19]. If the absorbing layer is not included, irrealistic signals can appear.

Research in acoustic propagation shows the FDTD method can approach wave propagation in 2D with many reflective objects placed in the geometric environment [21, 22] (urban acoustics) and [23] (room acoustics).

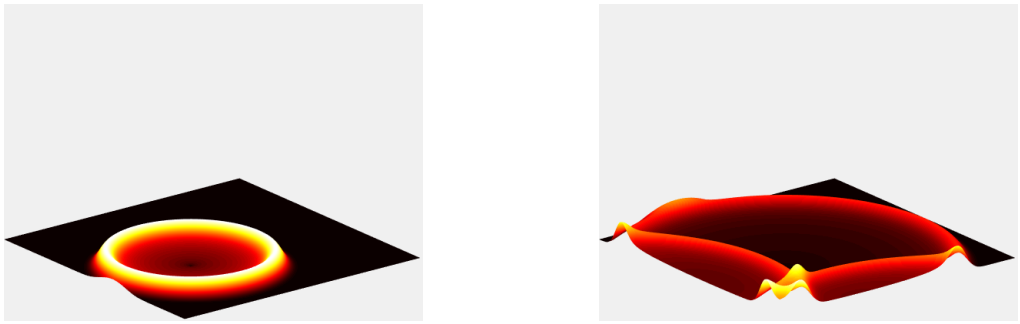

Figure 4-3: 2D FDTD simulation with edge as reflective boundary [20]

Stability criterion The FDTD method is sensitive to fluctuation - it destabilizes easily, resulting in transients which are not present in the real scenario. Destabilization can be prevented when the stability criterion is met and the dispersion error is minimized. The stability criterion is expressed by the Courant condition for 2D and 3D [19]:

$$\Delta t \leq \frac{h}{\sqrt{2}c} \text{for 2D} \qquad \Delta t \leq \frac{h}{\sqrt{3}c} \text{for 3D} \tag{4-10}$$

With h the spacial grid size, Δt the time step and c the wave phase-speed.
Evidently, FDTD simulation is limited by these variables. With too-high frequency and infinitesimal wave-length simulation with FDTD would become very CPU (or GPU) intensive [19].

4-4-3 Pseudo-spectral Time-Domain

More recent research compares application of Pseudo-spectral Time-Domain (PSTD) simulation to the FDTD method [24]. The PSTD method allows coarser subdivision of the modeled domain compared to the FDTD method for many situations and results in less computation time [25].
An example of PSTD simulation is shown in Figure 4-4.

Figure 4-4 shows how 3D simulation can be visualized by inserting only important cross-sections of the third dimension.

4-4-4 k-Wave method

The k-Wave is a variation of a PSTD approximation to, in this case, a generalised form of the Westervelt equation. Resulting in three coupled equations which are solved by the k-space pseudo-spectral method [27].

In order to simulate a time-varying source, the signal needs to be filtered in order to avoid aliasing in the spatial domain and time domain. Aliasing poses a problem in both domains,

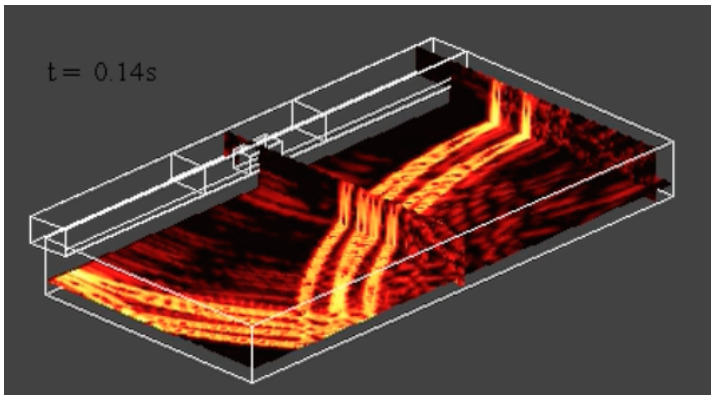

Figure 4-4: PSTD method simulation in a gym - openPSTD software [26]

because propagation is simulated in space and time. Figure 4-5 shows an example of the filtered signal (a linear chirp with 0kHz-50kHz frequency sweep and unfiltered pressure amplitude of 10 Pascal). These properties are picked for visualisation purposes.

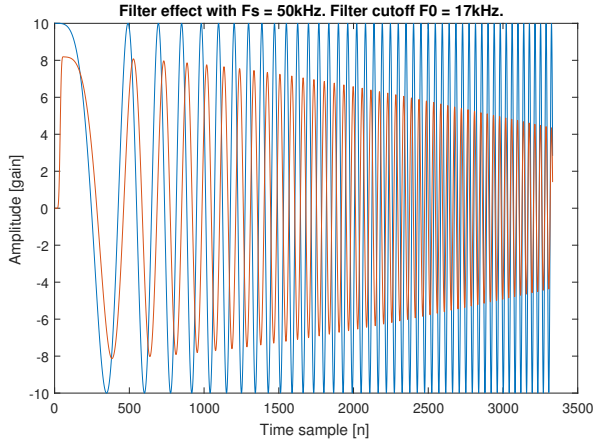

Figure 4-5: Filtered chirp signal before simulation - k-Wave toolbox [28]

Figure 4-5 shows that the highest frequency of the chirp signal is not attenuated enough. The effect is visible in the simulation example in Figure 4-6. The signal shows slight aliasing in the spatial grid.

Simulating this geometry is therefore strongly limited by the 2D-Courant condition, given in equation 4-10. The trade-off is between sampling frequency (preventing frequency aliasing), geometry size (trade-off realistic simulation) and geometry spatial division (preventing spatial aliasing).

4-5 Model verdict

Section 4-1 and Section 4-4 presented three approaches to modelling an acoustic channel with both advantages and disadvantages. The requirements from Chapter 2 determine which

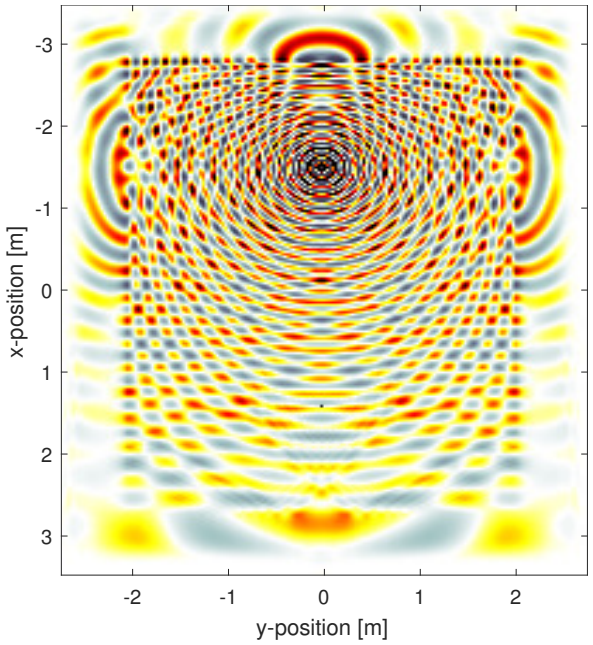

Figure 4-6: Simulation of a domain with reflective boundaries. The point source is at [-1.5m, 0m]. The point receiver is at [1.4m, 0m] - k-Wave toolbox

model will be used. To provide more constructive comparison between these models, their common properties are summed up.

4-5-1 Ray method

The Ray method is primarily limited by the computational load caused by the order of reflections and the amount of determined eigenrays. Applying the impulse response estimation, given by equation 4-2, requires the absorption model, path attenuation model, path delay and reflection coefficient model. It is capable of determining the channel impulse response independent from the input. This method allows to model static variables, it presents the source and receiver with a known location and requires a specific geometry as input.

However the impulse response estimation method does not allow the source and receiver to move in space and time, but it estimates the channel in the frequency domain dependent on path attenuation and reflection attenuation. Therefore the Doppler effect, as discussed in Section 3-3, can not be modelled with this simplified model. A source with static, constant velocity could still be implemented by post-analysis of each ray path and frequency-stretching of each path before it is summed in the impulse response series.
As proven in Section 3-3, the static Doppler effect is negligible. The effect of dynamic Doppler shift due to acceleration, however, is not yet quantised. It is assumed that acceleration greatly distorts the input signal because of it's non-linearity. The impulse response estimation method is not suitable for modelling this effect.

	FDTD	PSTD	Ray	Comments
Speed	- -	-	++	Ray method doesn't involve simulating whole grid.
Shear	- -	-	+	Shear wave calculation increases computational load.
Doppler	+	++	- -	Ray method does not allow a moving source
3D	+	+	++	3D intensifies calculations (same as speed).
2D	+	+	++	2D calculations are feasible for limited bandwidth,
Impulse estim.	-	-	++	FDTD/PSTD require non-ideal impulse approximation or deconvolution.
Max signal Bandwith	- -	-	++	Ray method allows sampling frequency higher than 500kHz.
GPU/CPU optimizable	+	+	-	FDTD/PSTD toolboxes are often optimized for parallel processing.
Approx reality	++	++	+	Ray approximation vs real wavefront simulation.

Table 4-1: Trade-off table for FDTD method and PSTD method and Eigenray approximation. The k-Wave toolbox is represented under PSTD since it has generally the same properties.

4-5-2 k-Wave PSTD

Since the kspace pseudo-spectral time-domain method models the wavefronts in time and space by defining a grid division in these domains, the model is primarily limited by signal bandwidth, wave-length, phase-speed and thus spatial resolution. This means modelling in 2D or 3D will strongly affect the computational load.
The static and dynamic Doppler effect can be modelled by a position-velocity profile as initial conditions without extra computational load, since the point source simply travels the grid points in stead of taking a constant position. This model is therefore suitable for dynamic Doppler effect simulation.
Since this model gives an output signal instead of the channel response, either channel deconvolution is required in order to acquire the channel impulse response or an approximation to a system impulse needs to be found. Both approaches pose another layer of complexity and possible error.

4-5-3 Model choice

Table 4-1 summarises and qualifies the previous disadvantages and advantages by giving *'++'* to a great advantage, *'+'* a moderate advantage, *'-'* to a disadvantage and *'- -'* to not applicable.
The resulting verdict is to use the impulse response estimation by eigenray estimation, because it presents much less computational load, allows a much higher channel sampling frequency, approximates reality almost as well as FDTD/k-Wave, does not require system deconvolution or impulse approximation and allows 3D simulations without any major impact.

Chapter 5

Model Implementation

The impulse response estimation method described in Section 4-2 proved to be the most suitable for implementation. To be able to implement this method several steps need to be taken or variables calculated. Figure 5-1 shows this in functional form.

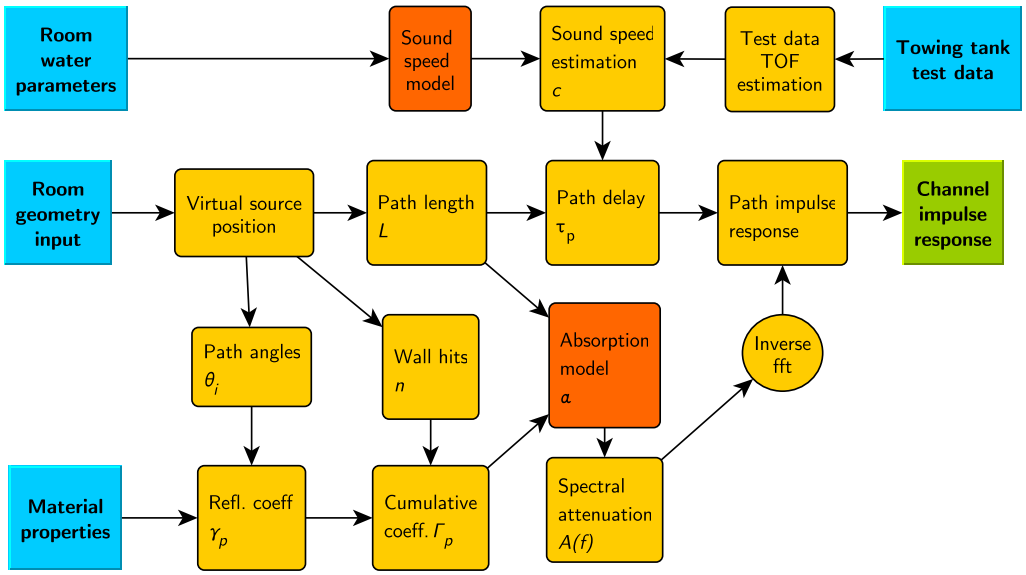

Figure 5-1: Functional breakdown of the model. Blue box: input. Green box: output. Orange box: empirical model.

Figure 5-1 shows three inputs: room geometry parameters, water parameters and reflective material parameters. These parameters are branched in such a way that the following model variables are calculated (in logical order):

- Path length L

- Path delay τ_p
- Sound speed c
- Angle of incidence θ_i
- Reflection coefficient γ_p
- Cumulative reflection coefficient Γ_p
- Absorption $A(f)$
- Transfer function (Inverse FFT)
- Channel impulse response

The path length, path delay, angle of incidence and reflection coefficient are calculated through the image-source method, which is an algorithmic approach to finding the eigenrays connecting source and receiver. The result is a set of virtual sources, expressed in virtual rooms. These virtual rooms simplify the structural problem of calculating the amount of reflections and angles of incidence.

5-1 Image source method

To determine the path lengths, the test environment, the 3me towing tank, is modelled as a rectangular box as shown in Appendix B. The geometry of the towing tank allows this approximation, since it does not have significant deviation from a cuboid room. To determine the path lengths from this geometry the image source method [9] is used, which is shown in Figure 5-2.

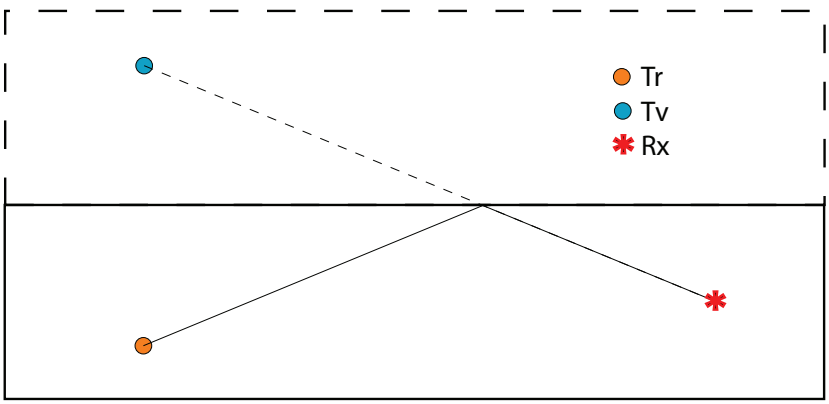

Figure 5-2: Image source method. Tr is the real source, Tv is the virtual source and Rx is the receiver

An eigenray transmitted from the transmitter, Tr, is reflected from the upper boundary and received by the receiver, Rx. From the receivers point of view it seems the transmitters position, Tr, is 'behind' the wall at the virtual source position Tv. The transmitter is mirrored at the upper boundary.

The image source method can also be used for the other walls/sides and even for corner 'rooms', as shown in Figure 5-3. The Figure shows the virtual sources for 5 virtual rooms and the eigenrays. The diagonal rooms are second order reflections, the rays corresponding to these virtual points interact with the walls twice, as can be seen in the Figure. This reflection

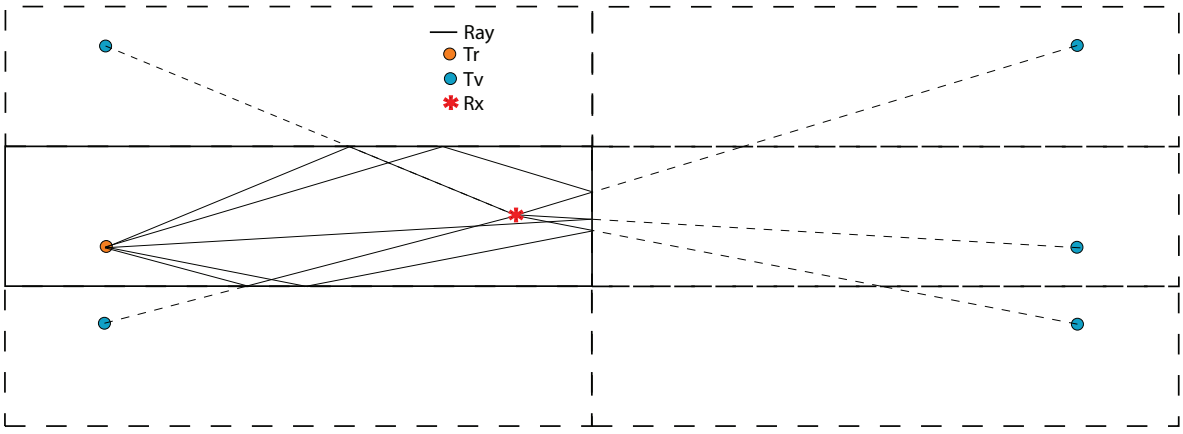

Figure 5-3: Virtual sources for 5 virtual rooms. The paths of the eigenrays are also shown. The top right and bottom right room contain a second order reflection

map or image source method can be extended to any arbitrary number of reflections in any direction. This method can also be extended to 3 dimensions. The next step is to implement this method in Matlab.

5-1-1 Virtual source positions

The goal is to determine the virtual source positions. From this the path lengths and angles can be determined. In Figure 5-4 one can see two virtual sources. The receiver is not shown because the virtual positions of the source are independent from the receiver position. To calculate the virtual source positions a reference point is needed. The bottom left corner is taken as the origin (see Appendix B). The virtual sources have the same x coordinate because they are mirrored in the y direction. To determine the y coordinate a indexing grid is introduced identifying the position of the virtual room. The variables (i, j, k) are a set of indices belonging to each virtual room in the (x, y, z) direction.

For example, the variable j denotes the virtual room index in the y direction. The y coordinate of the first virtual source y_1 is equal to $\mathrm{y}_1 = 2W - \mathrm{y}_0$ and the coordinate $\mathrm{y}_2 = 2W + \mathrm{y}_0$. Thus depending on whether j is even

$$\mathrm{y}_j = (j * W) + \mathrm{y}_0 \tag{5-1}$$

or odd:

$$\mathrm{y}_j = (j + 1) * W - \mathrm{y}_0 \tag{5-2}$$

This also applies for negative values of j and the same principle applies for the x and z (resp. i and k) directions. This results in the image in Figure 5-5 for the 2 dimensional case. The expansion of the grid is limited to the number of reflections resulting in a rhombus shaped grid in the 2 dimensional case and a diamond shaped grid in the 3 dimensional case. In Figure Figure 5-5 the eigenrays are limited to 3 reflections. In Figure 5-6 the virtual sources are shown for the 3 dimensional case. The test environment, the towing tank, is shown as a

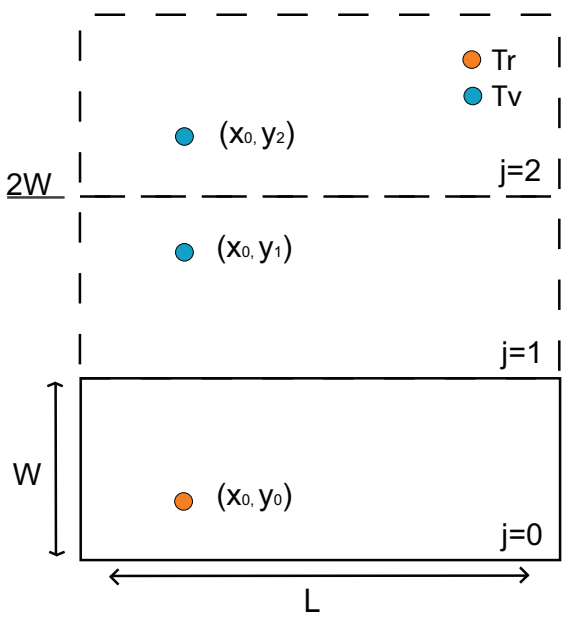

Figure 5-4: Tr is the actual source, Tv is a virtual source. W is the width of the room and L is the length of the room

yellow rectangular box. The virtual sources are shown as blue dots. For clarity the size of the tank is reduced to have a length of 10 meters.

5-1-2 Adapting to harbour environment

The towing tank has a length of 142 meters, a ray transmitted from a corner of the tank will be reflected from the other side of the tank and travel all the way back to the receiver (depending on the receivers location). Signals that have travelled this long will be strongly attenuated compared to the direct path and arrive much later, therefore these are of less interest. In case of a more realistic harbour environment not all the walls need to be in place, one or more sides might be absent. In this case the expansion of the reflections is simplified. If one side is missing the signal can only reflect once from the opposite boundary. This is illustrated in Figure 5-7. The wall at x = 10 meters is absent. Therefore, the rays can only reflect once in the x direction from the wall at x = 0 m. In both Figure 5-7 and 5-6, 3 reflections are shown, the difference is clearly visible.

The model implementation for the Fleet Cleaner harbour environment might require a non-rectangular geometry as assumed throughout this section. This is proposed and discussed further in Section 6-3.

5-2 Path lengths

The distance the ray has travelled from the source to the receiver, the path length, can be determined from the virtual sources position and the receivers position. Given a virtual source

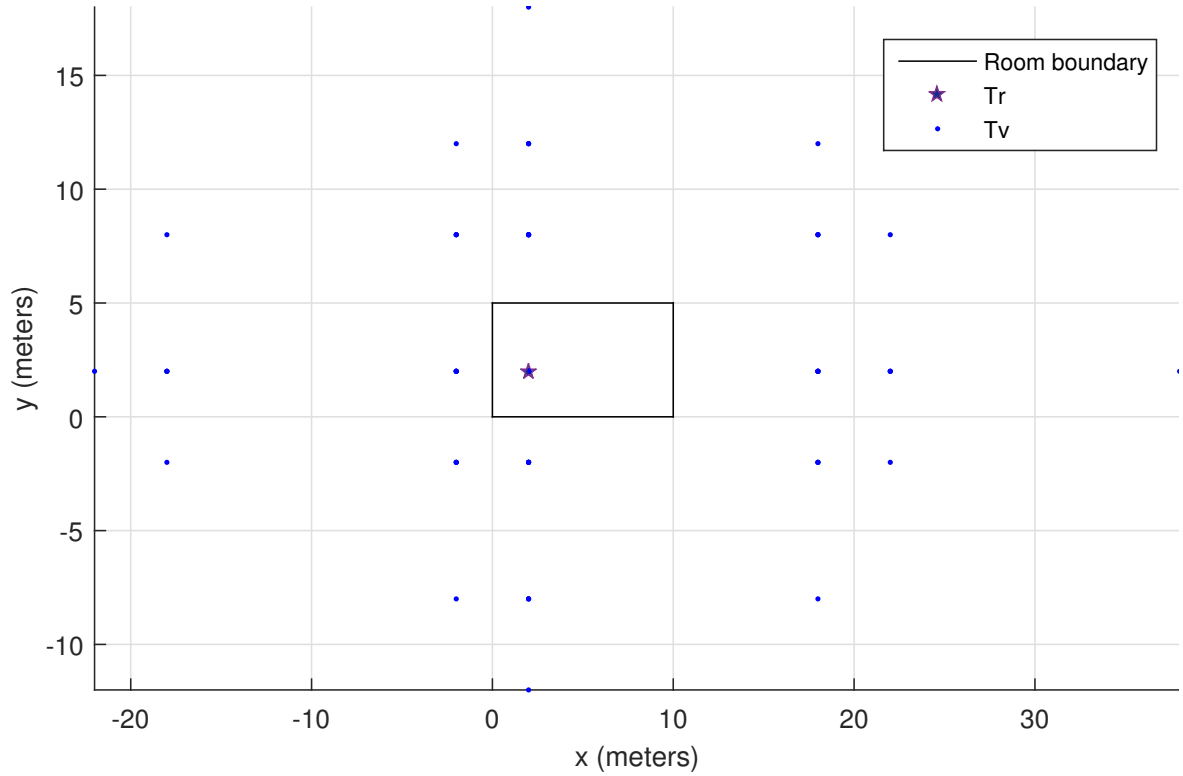

Figure 5-5: The virtual points for 3 reflections. Tr is the real transmitter, Tv are the virtual sources.

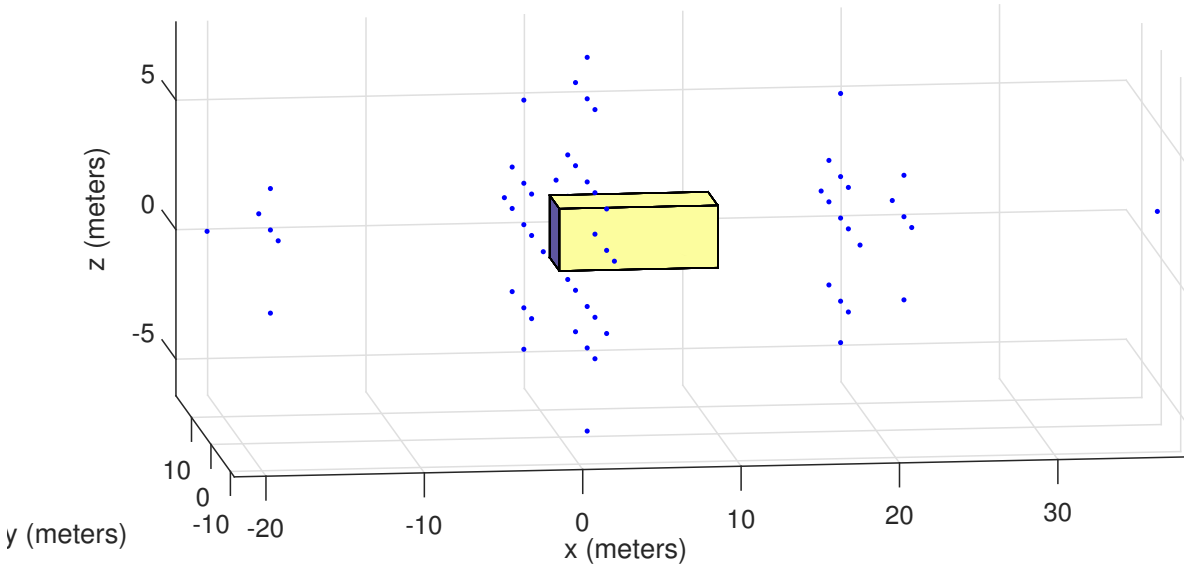

Figure 5-6: The virtual points for 3 reflections in 3 dimensions. The yellow rectangular box is the modelled towing tank. The blue dots are the virtual source positions

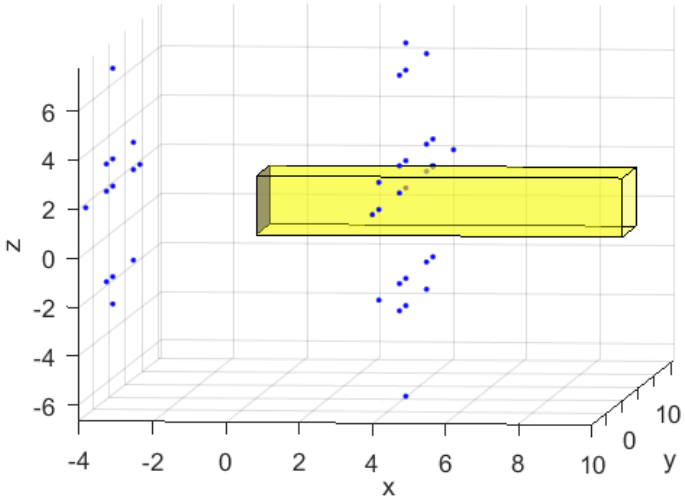

Figure 5-7: Virtual sources for 3 reflections. The wall on the right side, at x = 10 meter, is absent. The blue dots represent the virtual sources.

position (x_j, y_j, z_j) and the location of the receiver (x_r, y_r, z_r) the distance or path length can be calculated using the following equation:

$$l_p = \sqrt{(x_r - x_j)^2 + (y_r - y_j)^2 + (z_r - z_j)^2} \tag{5-3}$$

5-2-1 Path delays

The delay for each path can be determined by Equation 4-6, which requires a speed of sound $\tau_p = l_p/c$. l_p is the eigenray path distance.

5-2-2 Sound speed

Two sound speed models have been stated in section 3-1. The Chen & Millero model was stated as more suitable for estimating the speed of sound. Table 5-1 present the chosen range for the sound speed estimation, since not all variables are known[1]. The values from this table are used in the model implementation shown in Appendix C-1. Resulting in a estimated sound speed of (1465-1470 m/s)

variable	Range	Units
S	[0, 5]	g/kg
T	[12, 18]	$°C$
z	[0, 2.5]	m

Table 5-1: Speed of sound parameters

Chapter 6 goes into more detail on comparing this estimation with measured data.

[1]The temperature of the towing tank was measured to be 15 degrees with an estimated deviation of 3 degrees due to the inaccurate thermometer.

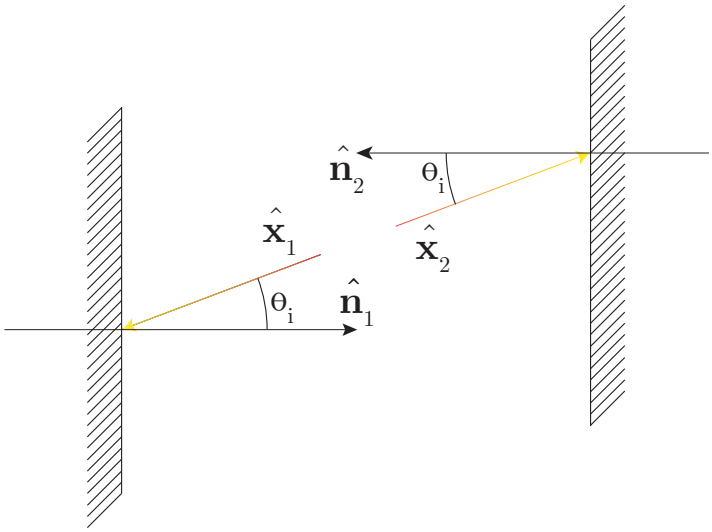

Figure 5-8: The Z-angle formed by two opposite boundaries.

5-3 Cumulative Reflection coefficient

A reflection coefficient for a multi-reflection path can be approached as the cumulative reflection coefficient Γ_p, which is required for the impulse response method, as discussed in Section 4-2. For this cumulative reflection coefficient the amount of wall hits is required and the angles of incidence for the angles to hit the boundaries.

$$\Gamma_p = \prod_{i=1}^{n} \gamma_i(\theta_1) \tag{5-4}$$

Where n is the amount of wall-hits of a multi-reflection path. Γ_p is dependent on θ_1, which is discussed below.

5-3-1 Angles

The angle of incidence between a boundary plane and the path vector can be determined by determining the normal vector to the plane. The angle between the normal vector and the vector then represents θ_i. Since the testing tank consist of six different walls, there are six boundary planes. Since a ray could reflect on all of these boundaries in one path, at least six incidence angles need to be calculated for the reflection coefficient of all boundaries. Figure 5-8 shows that two opposite boundaries must have the same angle of incidence θ_i. Therefore three angles of incidence are required.

The normal vector of the boundary assists in calculating the incidence angle. Since three angles of incidence are enough for the algorithm, only three normal vectors need to be defined orthogonal to one wall of the geometry.

$$\hat{\mathbf{n}} = \begin{cases} [1,0,0] & \text{for back, front plane} \\ [0,1,0] & \text{for top, bottom plane} \\ [0,0,1] & \text{for left, right plane} \end{cases} \tag{5-5}$$

The geometry definition accompanied with this coordinate system is presented in B. To calculate the angle between the path vector $\hat{x}$ and normal vector $\hat{n}$, $\hat{x}$ must be projected onto $\hat{n}$ and the rejection $|\hat{x} \times \hat{n}|$ must be divided by that result. The incidence angle is then expressed with the following equation:

$$\theta_i = tan^{-1} \frac{|\hat{x} \times \hat{n}|}{\hat{x} \cdot \hat{n}} \tag{5-6}$$

Where $\hat{x}$ and $\hat{n}$ are respectively the corresponding path and normal vector from Figure 5-8. θ_i is an angle with domain [-90°, 90°] due to the domain of $tan^{-1}(x)$. The next section uses the incident angle to calculate the reflection coefficient.

5-3-2 Reflection coefficient

Section 3-2-4 stated four equations for the reflection coefficient at elastic and solid boundaries, which incorporated longitudinal and shear wave reflections, of which most are elastic and one is not elastic: concrete, steel and air (non-elastic). For example, the water surface is a boundary between water and air. At this boundary the reflection coefficient can be approached as a 180 degrees phase change without loss. The reflection coefficient is thus: $\gamma_i = -1$ [9].

The reflection coefficient of other boundaries can be approximated by the parameters given in Table 5-2. These values might differ from reality.

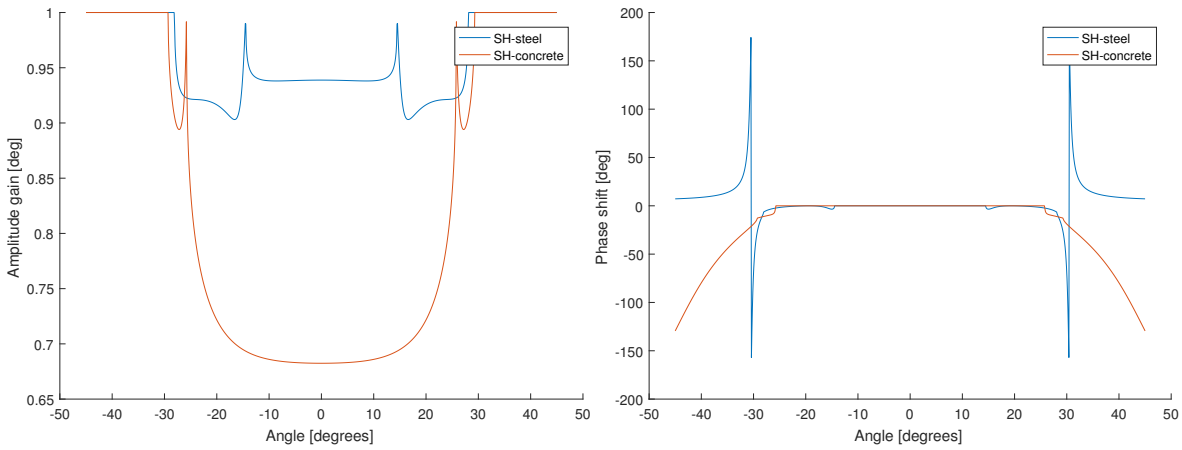

(a) Magnitude of reflection coefficient ($|\gamma|$). **(b)** Phase of reflection coefficient ($\angle\gamma$).

Figure 5-9: Magnitude and phase plot for realistic media as defined in Table 3-3. Note that the reflection coefficient is equal for negative and positive angles of incidence (symmetric).

Material	c_2	c_{shear}	ρ_2	μ_2	θ_c	θ_{cshear}
Steel	5920	3142	7900	$78*10^9$	14.5	28.08
Concrete	3400	3022	2300	$21*10^9$	25.8	29.31

Table 5-2: Example medium parameters for Figure 5-9 with shear waves.

Figure 5-9 shows how much difference the parameters make for different materials. This suggests the parameters for the boundaries determine greatly whether the model approximates test data in amplitude. Contradictorily, Chapter 6 shows that the steel boundary results in

a slight increase of the channel impulse response compared to concrete (Figure 6-7). Not all parameters are accurately known and are estimated and compared with assist of online repositories and literature [5, 1, 9].

5-4 Transfer function

Once the cumulative reflection coefficient Γ and the path dependent attenuation A_p are obtained the transfer function for the corresponding path can be determined, according to Equation 4-2. In Figure 5-10 the transfer function for a direct path with a length of 50 meters is shown, a distance associated with the Fleet Cleaner environment. The low pass filter effect is clearly visible, although the impact is minimal on this short range. The magnitude of the transfer function decreases slightly for increasing frequencies.

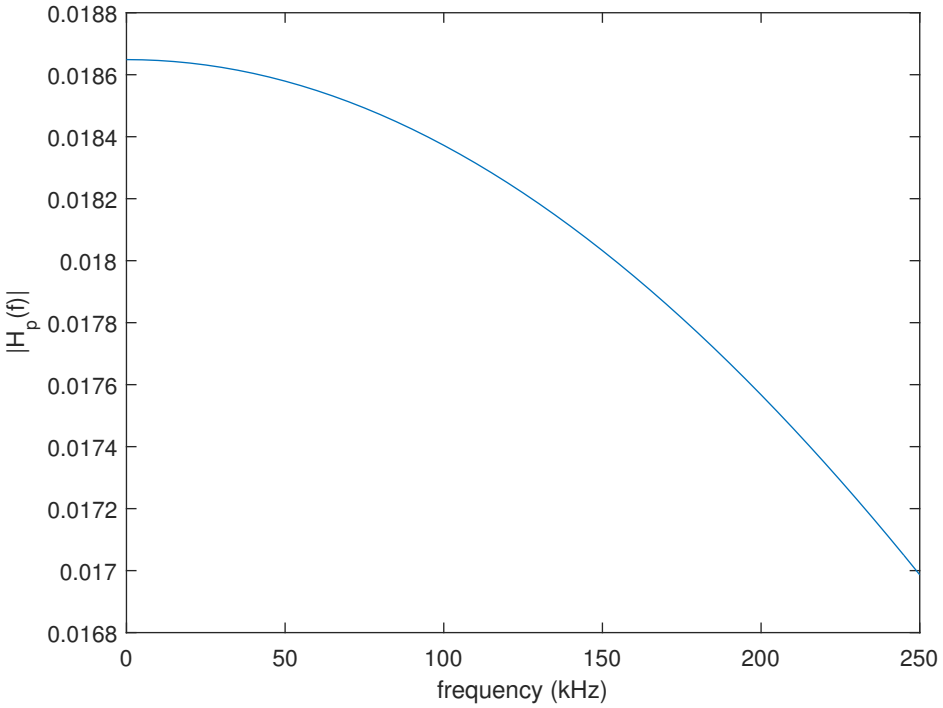

Figure 5-10: The magnitude of a transfer function $H_p(f)$ for a direct path with a distance of 50 meters.

To calculate the impulse response, the ifft (inverse fast Fourier transform) is used. The ifft requires a two-sided symmetrical spectrum as input to obtain an output signal corresponding to the 0 to 250 kHz range, this is shown in Figure 5-11. The corresponding impulse response obtained by applying the ifft is shown in Figure 5-12. The obtained impulse response is non-causal because only the magnitude of the transfer function is known, resulting in a zero-phase filter. The reference used [16], shows the path impulse responses obtained are non-causal before a time delay is applied. Figure 5-12 shows this as a symmetry around n = 1, due to the indexing of MATLAB, and because of the circular property of the ifft the remaining samples are placed at the end of the vector. If this impulse response is shifted in time the

symmetry becomes clearer. The corresponding impulse response for this time shift is shown in Figure 5-13a, the low-pass filter effect is emphasised in Figure 5-13b.

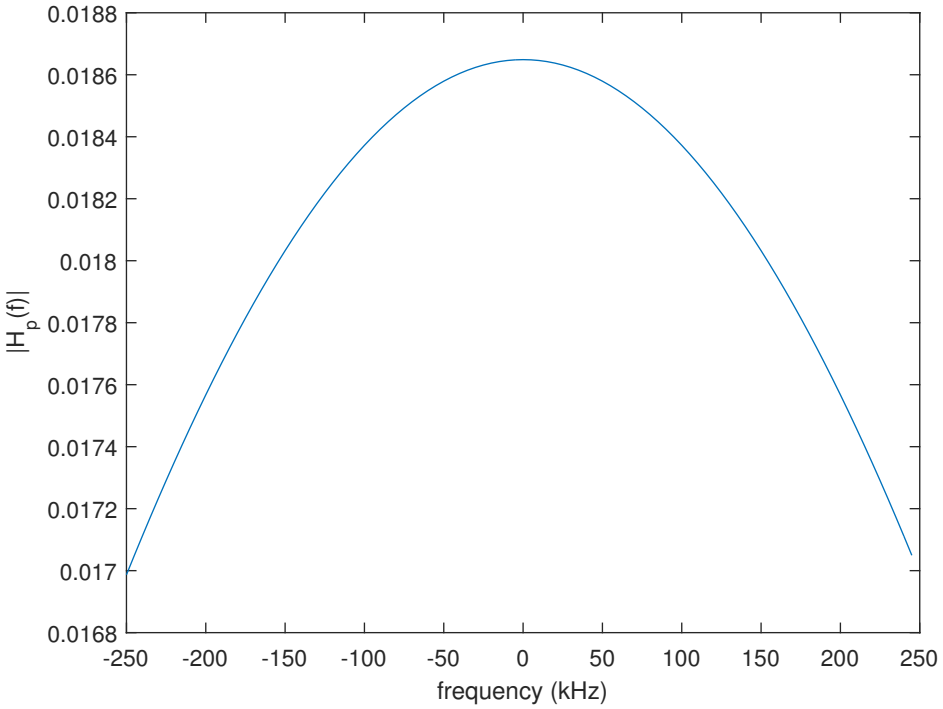

Figure 5-11: The two-sided magnitude of a transfer function $H_p(f)$ for a direct path with a distance of 50 meters.

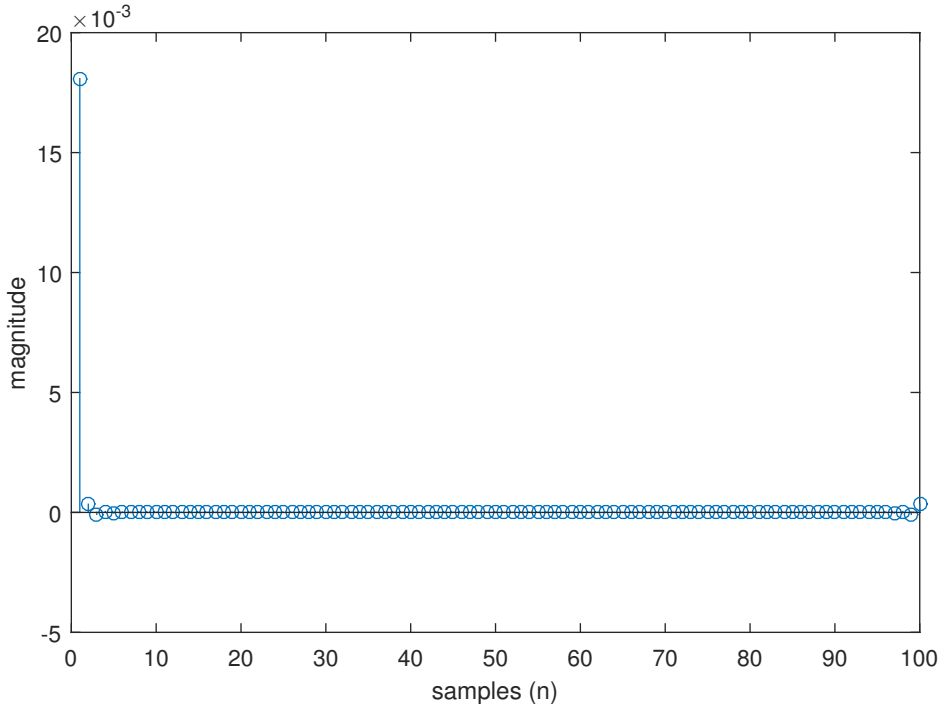

Figure 5-12: The impulse response obtained after applying the ifft

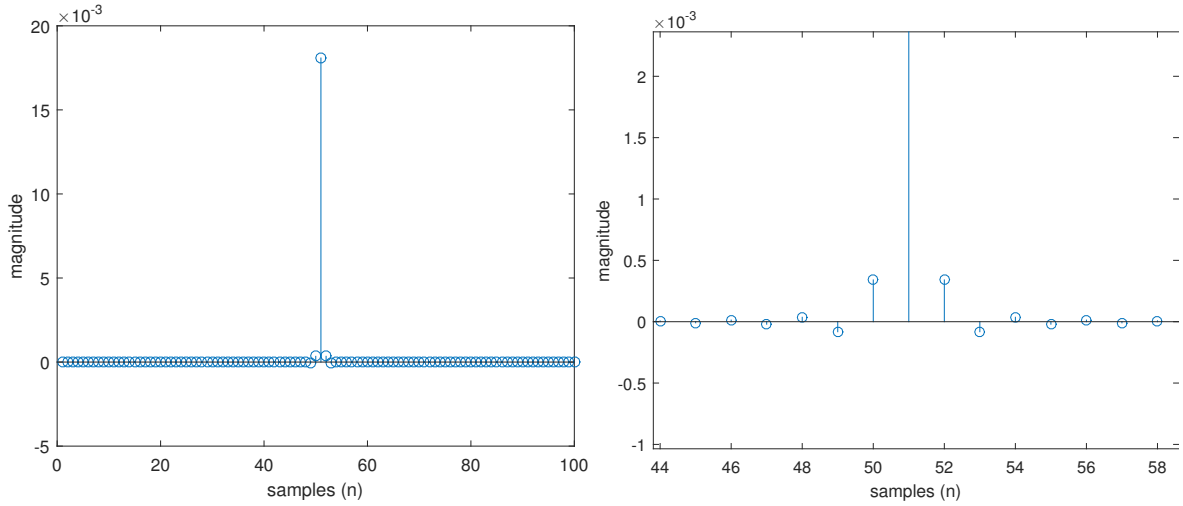

(a) The impulse response with a small lowpass filter effect

(b) Lowpass filter effect

Figure 5-13: The impulse response for a direct path of 50 meters

5-5 Channel impulse response

In the end all the individual path impulse responses are summed, according to Equation 4-5, to obtain the total impulse response of the channel. The time delays obtained from Equation 4-6 are converted to samples using the fact that one sample corresponds to $T = 1/Fs$. This causes a maximal quantisation error equal to a half of T, $e_{max} = 1/(2Fs)$.
Where e_{max} is the maximal quantisation error. For the sample frequency used, $500kHz$, this results in $e_{max} = 1\mu s$. This is an acceptable error considering the set requirement of obtaining the time of flights within $70\mu s$ precision.

An example of the obtained impulse response in shown in Figure 5-14. The receiver was at $(x_r, y_r, z_r) = (10.00m, 1.00m, 1.85m)$ and the beacon at $(x_b, y_b, z_b) = (35.00m, 1.00m, 1.85m)$. The Figure shows the impulse response for up to 40 reflections and is limited to $100ms$. Some peaks are much higher compared to others, this happens when two or more paths have the same delay and are thus summed up to obtain a higher peak. There is a strong correlation between the delay and the reflection order, this is visualised in Appendix D-1.

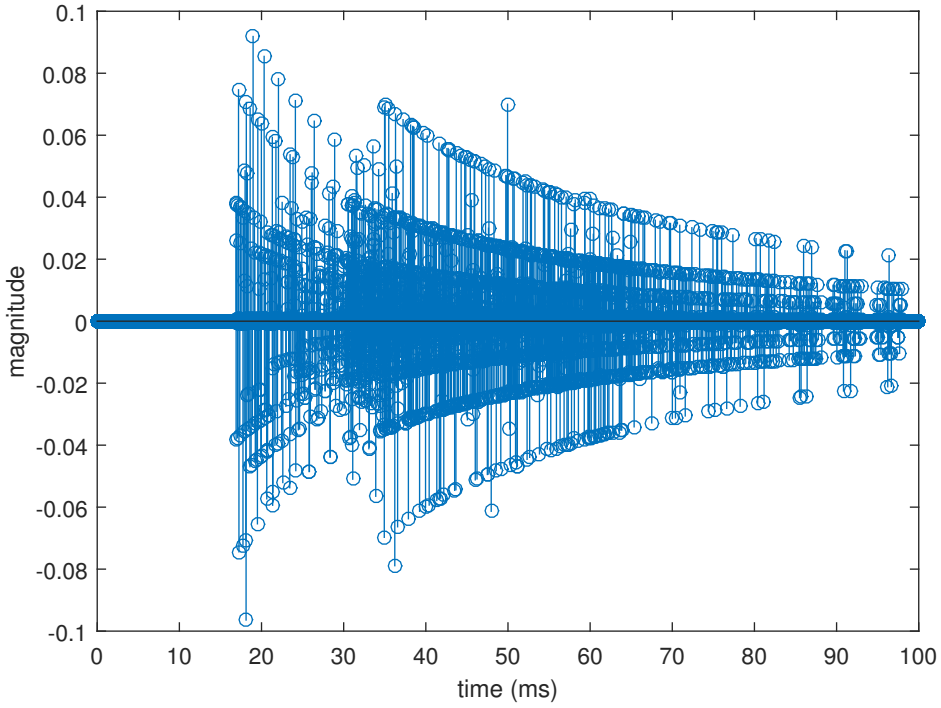

Figure 5-14: The channel impulse response for n = 40 reflections

Chapter 6

Validation

This chapter will approach validation of the model in three parts. In Section 6-1 the dispersion and attenuation are discussed and the determined impulse response is justified. In Section 6-2 the model is compared with measured data, this will use a channel estimation from the measured data for comparison. The results show that the model does come close to test data in Time of Flight after applying a sound speed correction. At last the validity of the model for a more realistic Fleet Cleaner environment is discussed in Section 6-3.

The channel model consists of various blocks shown in Figure 5-1 which cooperate to determine the channel response. The key components of the channel impulse response are the path dependent attenuation and the time of flights of the direct path and the different reflections, these are therefore the main priority of the validation. The reflection coefficients used are based on parameters found in literature, a comparison is made to see the influence of different materials on the channel response compared to the measured data. The combined work of the hardware models and channel model is discussed in more detail in [3].

6-1 Validation of attenuation and dispersion

This section goes into more detail about the attenuation due to distance travelled and compares it with the attenuation due to the expected low-pass filter effect of water (high-frequency absorption).

6-1-1 Attenuation coefficient

Figure 6-1 shows the path attenuation for 0 to $250kHz$ for a maximum of 15 reflections with a colour map. The Figure shows that longer paths (at path-index = 0, 400 and 900) relate to higher attenuation as well as a stronger low-pass filter effect. The yellow paths (longer distance) follow a curve which shows an increasing attenuation for higher frequencies. Although this filtering is present, the path length dependent absorption has more influence on the attenuation.

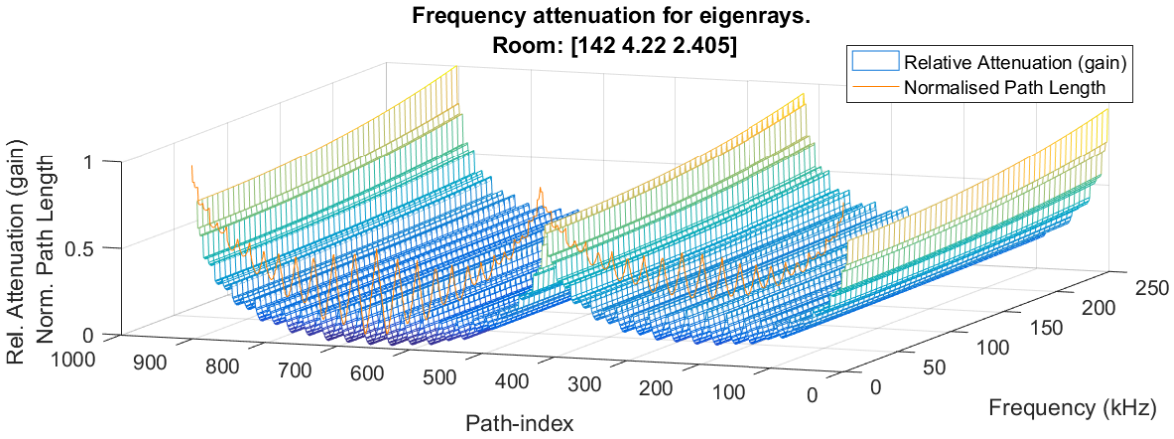

Figure 6-1: Normalised path attenuation and relative path length for frequency range [0Hz, 250kHz]. Yellow-coloured paths are more attenuated. Purple paths are attenuated little.

6-1-2 Dispersion & Absorption

The dispersion and absorption of the received signal have different effects as shown above. This section takes the modelled channel impulse response for one path and performs a convolution with a chirp signal. The dispersion impact for a chirp with a relative pressure amplitude of 1 as input, ranging from $40kHz$ at $t = 0ms$ and to $170kHz$ at $t = 10ms$, over 50 meters without absorption is shown in Figure 6-2, for clarity only the envelope is shown. The dispersion should result in a received signal with an amplitude of $1/(\sqrt{50^2 \cdot \alpha(f)^{50}}) = 0.02$ where α is unity for all frequencies, according to Equation 4-1. This matches with the expectations. In Figure 6-2 the same signal is shown but now with absorption. The expected amplitude with absorption, with α at $40kHz$ according to Figure 3-2b, is $1/(\sqrt{50^2 \cdot 1.0027^{50}}) = 0.0187$ and at $170kHz$ it is $1/(\sqrt{50^2 \cdot 1.0044^{50}}) = 0.0179$ which corresponds with the amplitudes in the Figure. The impulse response used has thus the desired effect, the attenuation is stronger for increasing frequencies. However the dependency on the frequencies considering the used chirp range bandwidth is minimal. The difference in gain between the used frequencies is $(0.0187 - 0.0179)/0.0187 * 100 = 4.3\%$. While the difference in gain compared to no absorption over 50 meters is $(0.02 - 0.018)/0.02 * 100 = 10\%$. The frequency dependency could thus be approximated as an extra constant gain for all frequencies.

In Appendix C-3 the envelope for a range of distances is shown for comparison.

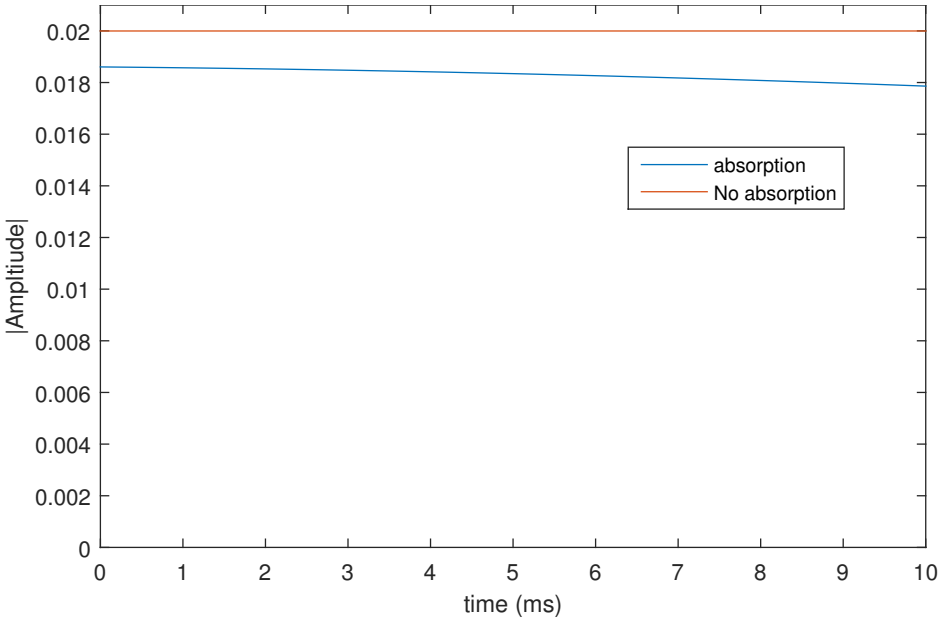

Figure 6-2: The envelope of the received chirp amplitude. Chirp ranges from $40kHz$ at t = 0ms to $170kHz$ at $t = 10ms$.

6-2 Validation through test data

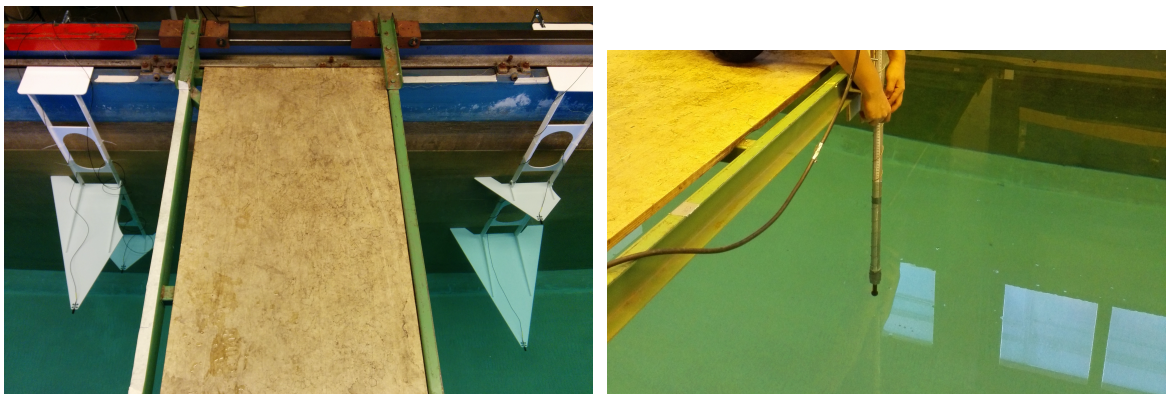

(a) Receiver setup **(b)** Transmitter setup

Figure 6-3: The transmitter and receivers in the towing tank

To validate the model, multiple measurements were done in the test environment, the 3me towing tank. One transmitter and four receivers were used in the test setup. The receiver setup is shown in Figure 6-3a and the transmitter in Figure 6-3b, the transmitter is the black dot at the end of the pole. About 200 measurements were done at different transmitter-receiver locations, including one transmitter and four receivers per measurement.
Appendix B shows the types of wall of this towing tank and the reference coordinate system with Figure B-1.

6-2-1 Chirp

A first validation of the results is done after the measurements by convolving the channel impulse response from the model with the transmitted chirp, ranging from 40kHz to 170 kHz with a duration of 10ms and comparing it with the received signal, see Figure 6-4. The characteristics of the transmitter, receiver and the final pre-amplifier are not taken into account in this Figure, the observed data is therefore scaled to fit with the model. This Figure illustrates the similarity between the acoustic channel model and the observed data. The location of the transmitter was $(x, y, z) = (31.00m, 0.5m, 2.31m)$ and the location of the receiver $(41.40m, 0.40m, 1.06m)$ resulting in a direct path length of $10.47m$. The second bunch of reflections, at $t = 50ms$, are the reflections coming from the steel plate in the towing tank (see Figure B-1 for the geometric definition).

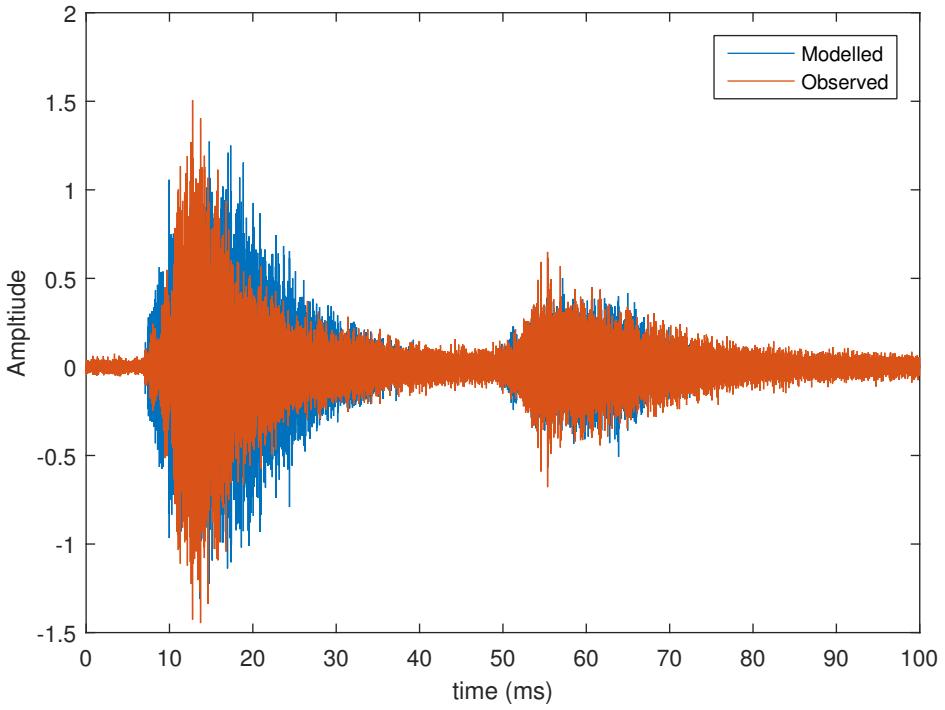

Figure 6-4: The modelled and observed chirp without compensating for hardware device responses. The observed chirp is scaled by 14 for comparison.

6-2-2 Channel estimation

A channel estimation is done on the measured data to compare the modelled channel impulse response with the estimated channel without the effects of acoustic hardware. This is achieved by different techniques involving estimating the hardware model and applying matched filter deconvolution to the received data resulting in a channel. A more detailed clarification to this mathematical approach is found in [3].

6-2-3 Sound speed estimation from measured data

Based on the expected salinity values (S = 0.5-3 ppt) and the measured temperature of $15°C$ a sound speed of 1465-1470 m/s was obtained. This sound speed showed an offset with the measured data. To obtain a more accurate speed of sound an estimation of the sound speed was done using the measured data. With four receivers and one beacon per measurement, 800 transmitter-receivers delays are available for determining the sound speed. This was done by filtering the peaks in the estimated channel using a simple peak detection algorithm. An example is shown in Figure 6-5. The TOF of the direct path is determined by $t = n_{peak}/Fs$ where n_{peak} is the position of the peak in samples. The speed of sound can then be determined according to $c = l_p/t$ where l_p is the known direct path length. Figure 6-6 shows the estimated speed of sound over all measurements. The result over all measurements is an estimated average sound speed of $c = 1478.7m/s$.

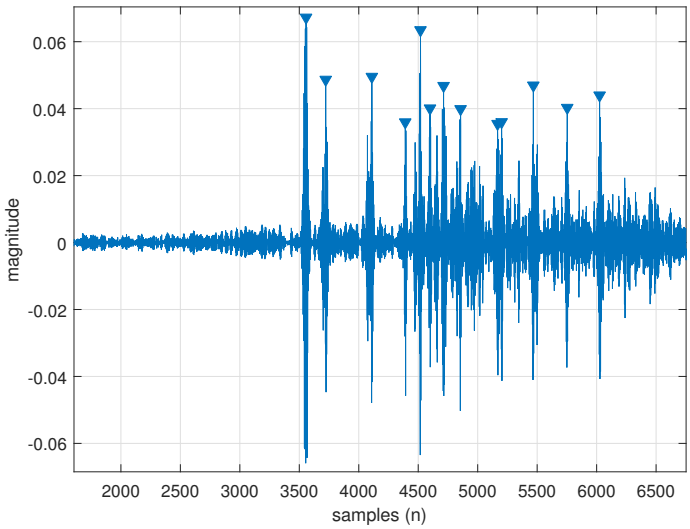

Figure 6-5: An example of the peak detection algorithm. The estimated channel corresponds with the observed chirp in Figure 6-4

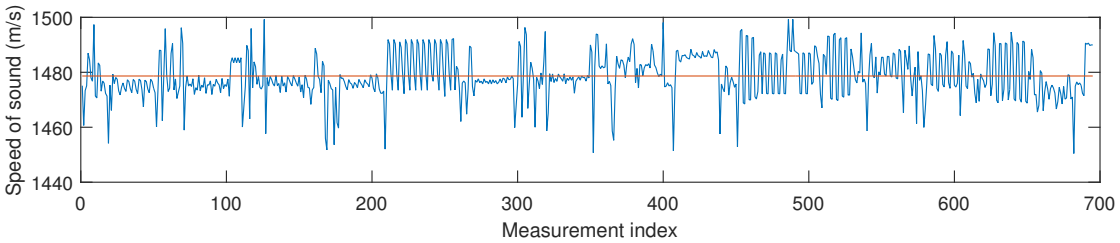

Figure 6-6: The estimated sound speed over all measurements using a simple peak detection algorithm. The red line is the average speed of sound.

6-2-4 Material properties

In Figure 6-7 the modelled impulse response is shown for two scenarios, one in case the wall at $x = 0m$ is concrete and the other for the case it is steel. One can see the reflections arriving at t = 55ms are the reflections coming from this wall. An increase of the impulse response is visible with the orange peaks appearing above the yellow peaks corresponding to respectively a steel and concrete wall. The parameters for steel and concrete used are the ones depicted in Table 5-2. Although these parameters are not determined exactly and a variation in the used parameters is possible, the increase in the channel impulse response is clearly visible. the environment the Fleet Cleaner robot will operate in contains a hull of a ship consisting of metal/steel thus this will have an influence on the Fleet Cleaner scenario. Figure 6-7 also shows that the sound speed estimation of Section 6-2-3 is accurate for this example, since the model shows impulse peaks closely to the arrival times of the two primary peaks of the observed data.

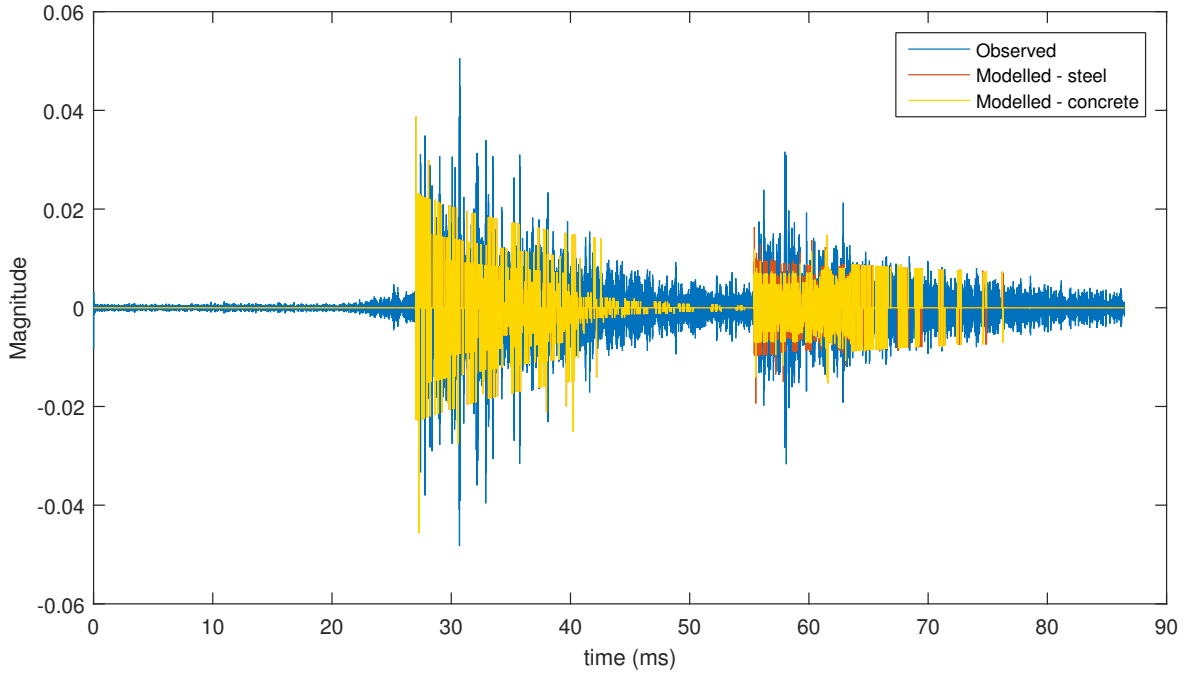

Figure 6-7: The modelled and estimated channel impulse response for the receiver at (x=21.00m, y=0.30m, z=1.85m) and the transmitter at (x=61.00m y=1.80m, z=2.31m). The steel wall is at x = 0m.

6-2-5 Comparing channel responses

The Figure in 6-8 shows the similarity between a modelled channel impulse response and an estimated channel impulse response. The first peak corresponds with the direct path, the following peaks are higher order reflections along the channel. The direct path and first and second order reflections, arriving between $3 - 6ms$ have the highest accuracy considering the time of flight. The higher order reflections have a higher deviation due to the uncertainty in the location of the transmitter and receiver and the uncertainty in the boundaries of the towing tank. These deviations are accumulated for every reflection. The hardware responses are included in the observed channel and as a result of this the observed data now only needs to be scaled by a factor of 3 to obtain the same direct path peak height. This scaling factor is probably caused due to deviations in the hardware models.

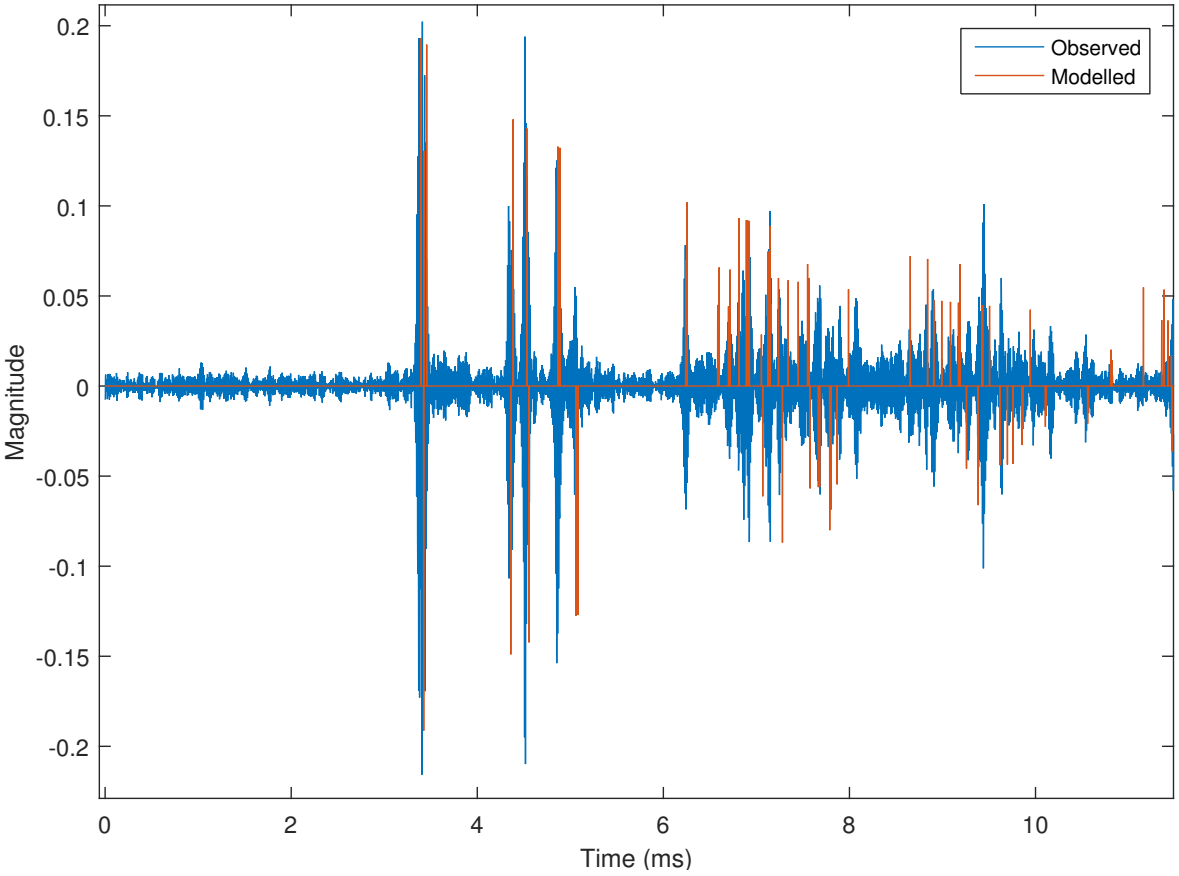

Figure 6-8: The modelled and estimated channel impulse response for the receiver at (x=21.00m,y=0.30m,z=1.85m) and the transmitter at (x=26.01m, y=0.40m, z=2.21m)

6-3 Adaption to a Fleet Cleaner model

The Fleet Cleaner environment will not consist of a rectangular uniform, which was the case in Chapter 5. Instead different dimensions and rotation of dimensions must be expected.

As shown in Section 5-1, the rectangular grid defined by virtual rooms have the advantage of simplifying the algorithm which determines the path-lengths, path-angles and thus reflection coefficients. It was not shown why the rectangular grid was chosen, except for the similarity with the geometry of the cuboid towing tank. Figure 6-9 sketches the changes made to the geometry structure of the towing tank towards a more realistic application geometry.

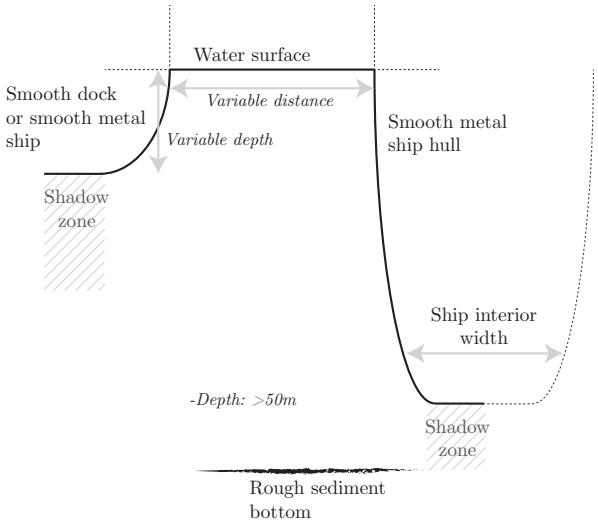

Figure 6-9: An approach to generalising the expected geometry of the Fleet Cleaner environment by a curved ship hull. The distances indicates with grey arrows are not exact and therefore kept variable. The shadow zone indicates the area where the hydrophones on the ship may or may not receive the signals from the robot properly anymore.

The curve hull of a ship is expected to be negligible for most of the ship's hull and can be approximated with a line. The curve of the nearby support ship or dock is more unpredictable, because the dock is expected to be rough non-curved material and the support ship much more curved since it will be much smaller than the to-be-cleaned ship.

6-3-1 Application - model adaptation concepts

As Figure 6-10a shows an geometry which keeps the image-source method suitable as ray method. The rectangular form of the grid is sheared, resulting in an approach which needs only minor alterations to the image source method.
Equation 5-6 in Section 5-3-1 defined three normal vectors to calculate three possible angles of incidence on the six reflective walls, defined in Appendix B.

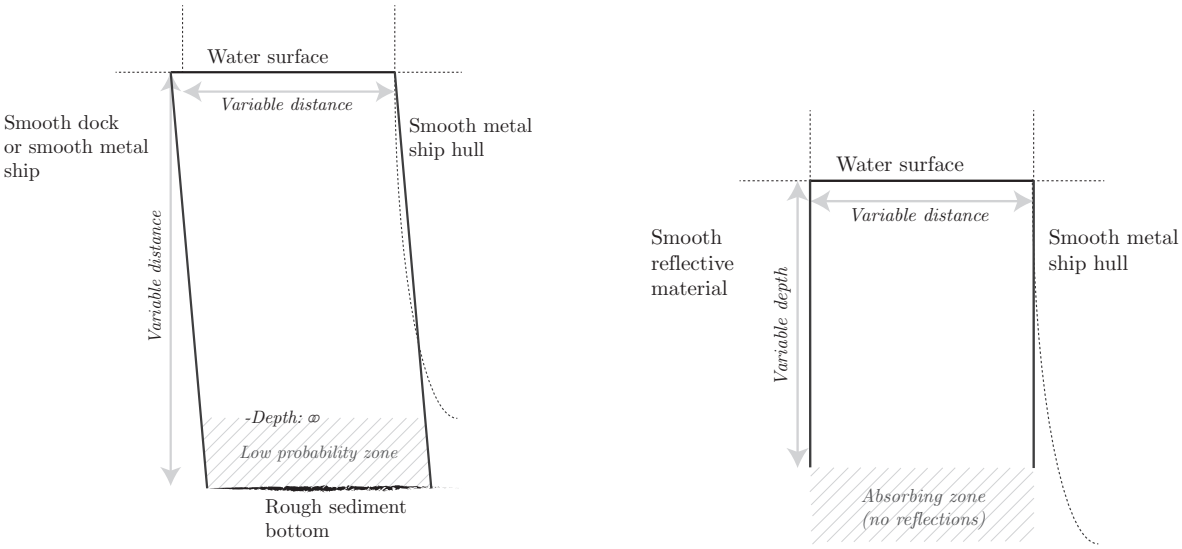

(a) Conceptual simplification 1 to Figure 6-9. The bottom is assumed strongly absorbing and scattering.

(b) Conceptual approach 2. Neglecting bottom reflection. Assuming two elastic walls.

Figure 6-10: Two concepts for approaching the harbor environment of the Fleet Cleaner robot.

When the grid is sheared by a certain angle as in concept 1 (Figure 6-10a), the normal vectors must be sheared with the same angle to keep the image-source method valid. This means the normal vectors are defined by equation 5-5 and a rotation transform on these vectors. Secondly, the mirroring technique presented in 5-1-1 changes to a warp transformation, which implements a shear transform on the virtual source. This is shown in Figure 6-11.
This shear warp is only an approach to implementing a tilted surface, because it assumes all surfaces to be equally tilted. Therefore concept 2 does not approach a tilted surface. Instead it assumes certain eigenray paths are never connecting a source and receiver, therefore one boundary becomes an absorbing medium.

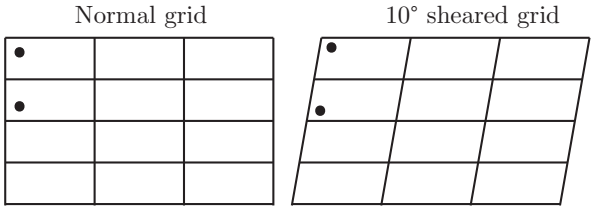

Figure 6-11: Shear warp of 10° on virtual rooms and virtual sources.

6-3-2 Shadowing and ray probability analysis

Concepts 1 and 2, shown in Figure 6-10 showed certain striped shadow zones. These represent lower-probability zones, where the chance of unobstructed (invalid) eigenrays is low.
The primary cause of this shadowing zone is the distance and thus the aborption caused by the depth of the bottom floor, which is assumed to be made up of sediment material. The second cause is the line-of-sight shielding caused by the curvature of the to-be-cleaned ship in those areas. There is no direct adaptation possible for the channel model to avoid the problem of shadowing. The third cause is the absorption of the bottom sediment layer, which is expected to be much higher than the concrete bottom of the towing tank (test environment). This sediment consists of fine to coarse grains of material (sand, mud, vegetation), which is less dense than concrete and steel. This implicates a lower reflection coefficient as is previously shown in Figure 3-3 (for low-density material). Aside from the reduced reflection coefficient; the assumption that the reflective materials are all elastic, hard materials is not valid for sediment material, which implicates sediment will absorb more energy as transmitted waves. Assuming this material to be an absorbing or negligible boundary is therefore logical. It remains to further research to confirm these three assumptions.
If the assumptions are valid, concept two is the most feasible attempt of representing reality with the eigenray model.

Chapter 7

Conclusion and recommendations

7-1 Conclusion

The used impulse response estimation method proved to be an efficient and accurate method for determining the channel response considering the static and precisely known geometry of the test environment, the towing tank at the faculty of 3mE of Delft University of Technology. The modelled channel comes close to observed data considering the Time of Flight accuracy, which was one of the key requirements.

However the adaptation to a more realistic Fleet Cleaner environment is less obvious. The image source method used to determine the eigenrays can be extended to simulate a more realistic Fleet Cleaner environment. This method requires an cuboid approximation of the harbour geometry or a sheared/warped cuboid approximation.

At the start of the project a priority list was made to determine the specifications of the model. The different elements the acoustic model had to have were all implemented. The model determines a channel response with the possibility of taking any arbitrary number of reflections and any transmitter-receiver location into account.

The frequency dependent absorption on the signal was implemented but the impact considering the frequencies and distances associated with the Fleet Cleaner environment was not very significant. For a distance of 50 meters a deviation in the gain with absorption compared to no absorption was 10% while the relative gain between the frequencies used, 40-170kHz, was only 4.3%.

The elements from the 'should have' column were partly implemented, the model has the capability to select variable material properties for the six boundaries associated with the image source method. The difference in reflection for concrete and steel is visible in the channel response.

Because the sound speed is an important aspect of the channel response an estimation of the sound speed was done based on observed data, obtaining a speed of sound of $c = 1478.7 m/s$ for the test environment. The resulting sound speed differed from the expected sound speed

based on a sound speed model which relied on the measured temperature. Shadowing zones and directivity were not implemented in the model, because the effects of these do not seem be of much influence for the used test environment.
Beam scattering, Doppler shift, noise source addition and a non-uniform geometry are not implemented because these do not have a high priority considering the test environment.

7-2 Limitations of final model

Multi-layer boundaries No attempt was done to model the boundaries as multi-layer geometries, since it was not expected to be of noticeable impact. A multi-layer boundary model has an effect on the reflection of waves. With a multi-layer reflection the model can predict delayed reflection of pressure waves deeper within the boundary. The disadvantage of multi-layer approximations is that it would make the image-source method more complex to implement and the geometrical properties of the boundaries would become unpredictable.

Scattering effects The model has the possibility to take any arbitrary number of reflections into account, but is only applicable in case the shallow water environment can be reduced to a cuboid shape. This is a limitation considering more realistic harbour environments. Besides the limitations in the geometry, the model considers all surface to be perfectly smooth and flat. To model scattering or diffusion on boundaries, stochastic analysis is required, which is not suitable to this deterministic model.

Moving source Doppler effect The model is not capable of modelling a moving source. The Doppler effect for a constant moving source was quickly calculated to be of minor influence. Test data shows also a minor influence on the channel response. Assuming the Doppler effect for *accelerated* motion is expected to have a major impact on the channel, but no linear mathematical transformations exist to incorporate this effect. Therefore this is a major limit of the model.

Shadow zones, illegal eigenrays The model is implemented with the assumption that all eigenrays arrive at the receiver, but not all paths might be valid. For example, placing objects in the line of sight of receivers or transmitters is not incorporated in the model. The advantage of being able to model the line-of-sight is to be able to predict when the Fleet Cleaner robot will receive only a reduced amount of usable signal for localisation.

The model limitations summarise as follows:

- More detailed boundaries make the model implementation much more complex.
- Scattering effects are not taken into account.
- Constant and accelerated motion Doppler effect can't be incorporated.
- Shadow zones are not calculated and used.
- Eigenray validation/probability analysis is not implemented.

7-3 Recommendations

The modelled received signal is attenuated by medium absorption, radial dispersion (distance travelled) and the frequency attenuation of the medium. The frequency dependency becomes relevant for longer distances and higher frequencies. Since the dispersion has a much stronger impact for the same distance, it is recommended to neglect the frequency dependency for the chosen signal bandwidth of 40kHz-170kHz and approximate it with a constant gain for all frequencies.
The absorption model used is applicable for a Fleet Cleaner environment and shows an even stronger absorption for all frequencies for a higher salinity which is the case in the Fleet Cleaner environment. Therefore the absorption cannot be omitted but could be approximated as a constant gain over all frequencies.

The model as it is can be extended to a more realistic harbour environment to a certain extent. To be able to model different geometric shapes/objects a different approach has to be taken. To do this a ray tracing approach might be more useful. This allows to analyse all kinds of geometries at the cost of significantly increasing the complexity and possibly the computational load of the model.
The kspace PSTD method is another option for simulating more complex behaviour, accepting the fact that the computational load is much higher. The k-Wave toolbox is developed to the extent of allowing: accelerated or constant Doppler effect, 2D or 3D simulations, multi-layer approximations, frequency attenuation models, non-point sources/receivers and shear wave reflections. Because this method becomes increasingly more intensive for a bigger grid it is recommended to input a limited range geometry as model of the harbour-environment for pre-analysis of shadow zones with limited line-of-sight and the sensitivity for accelerated Doppler movement.

The application model must be able to generate predicted channels at real-time frequency or even higher. Therefore it is not recommended to apply PSTD models for real-time simulation. For real-time analysis, it is recommended to limit the eigenray model with image-source method to a small amount of reflections and applying probability analysis to retrieve standard patterns of Time-of-Flight data. This will improve localisation with only one Time-of-Flight or Time-Difference-of-Arrival as discussed in [3].

Appendix A

Project Requirements

The project is split up into hardware models, acoustic propagation models and validation. The following requirements set the prerequisites for the design of these sub-models.

Functional requirements

R1 All sub-models, the hardware models and the acoustic propagation model, must be compatible and possibly be combined into one simulation model.

R2 All sub-models must be able to aid in localisation when combined.

R3 Time of Flight estimates must have an accuracy of 70 microseconds or less[1].

R4 The acoustic model must determine a channel impulse response.

R5 Model input signal bandwidth must be under 250 kilohertz, and coincide with the optimal working ranges of the used hardware and channel.

R6 Accuracy of hardware models must be within 1dB of magnitude compared to datasheet information and measurement data.

R7 Hardware model must only model the specific hardware made available by Fleet Cleaner.

R8 Acoustic model must have a simulation time of less than 30 seconds.

R9 Acoustic model must be able to model reflective paths.

R10 Acoustic model must model the geometry of the towing tank[2].

R11 Acoustic model must take material properties into account for each boundary (surface and walls).

[1] 70 microseconds corresponds to a 10 centimetre accuracy approximately.
[2] The large towing tank of 3mE.

R12 Acoustic model must model in 3D.

R13 Acoustic model must take arbitrary source and receiver positions in the towing tank into account.

R14 A feature extractor[3] to be used on the observed data must be designed.

Ecological embedding in the environment The ecological aspect of a software package is not directly visible, but the application of such software might create problems with ecology. For example, producing acoustic signals in offshore areas could threaten the habitat of nearby nautical creatures. This effect is less present in shallow-water harbour environments.

System Requirements

R15 The software must be delivered as a Matlab toolkit.

R16 The toolkit must function on Matlab 2012a and more recent versions.

R17 Individual parts of the toolkit must be accessible to the end-user.

R18 The software package must be fully accessible through a command interface.

Development of manufacturing methodologies

R19 The operational software must be developed in Matlab.

Liquidation and recycling methodologies N/A

Business strategies, marketing and sales opportunities

R20 The toolkit will initially be delivered to Fleet Cleaner exclusively.

R21 The toolkit will be under a five year embargo.

[3] A feature extractor offers at least channel estimation.

Appendix B

Geometry definition

Figure B-1 shows the definition of the towing tank geometry in this thesis. The types of boundaries are indicated. Note that the water surface represents a boundary from water to air. The reflective wall to the right is not defined, since it is considered absorbing.

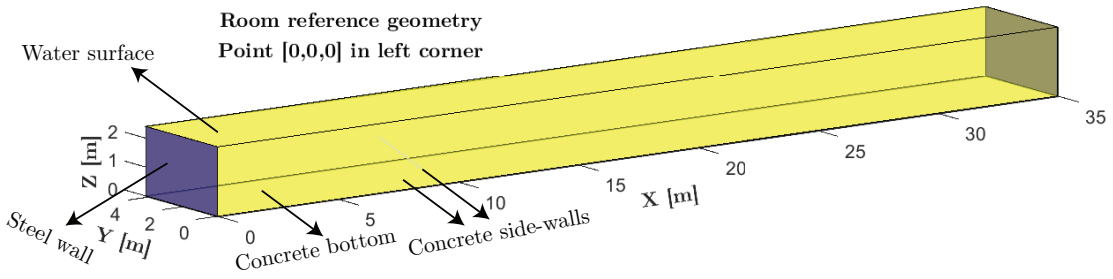

Figure B-1: Plot of the geometry definition and the walls for the image-source algorithm.

Appendix C

Complementary model information

C-1 Chen & Millero sound speed model

The following MATLAB code implements the sound speed model used for this thesis:

```
% UNESCO approved sound speed model - Tested with Matlab 2015/2016.

    % T := temperature vector [deg.]
    % S := salinity vector [ppt]
    % z := depth [m]
    n = 100;
    T = linspace(12,18,n);
    S = linspace(0,5,n);
    z = 0;

    rho = 998;  % kg/m^3
    g = 9.81;   % m/(s^2)
    P_pascal = rho * z * g;
    P = P_pascal * 1E-5; % Pressure [bar]

    c0 = 1402.388+5.03711.*T-5.80852E-2.*T.^2+3.3420E-4.*T.^3 ...
        -1.47800E-6.*T.^4+3.1464E-9.*T.^5;
    c1 = 0.153563+6.8982E-4.*T-8.1788E-6.*T.^2+1.3621E-7.*T.^3 ...
        -6.1185E-10.*T.^4;
    c2 = 3.1260E-5-1.7107E-6.*T+2.5974E-8.*T.^2-2.5335E-10.*T.^3 ...
        +1.0405E-12.*T.^4;
    c3 = -9.7729E-9-3.8504E-10.*T-2.3643E-12.*T.^2;
    A0 = 1.389-1.262E-2.*T+7.164E-5.*T.^2+2.006E-6.*T.^3-3.21E-8.*T.^4;
    A1 = 9.4742E-5-1.2580E-5.*T-6.4885E-8.*T.^2+1.0507E-8.*T.^3-2.0122E
        -10.*T.^4;
    A2 = -3.9064E-7+9.1041E-9.*T-1.6002E-10.*T.^2+7.988E-12.*T.^3;
    A3 = 1.100E-10+6.649E-12.*T-3.389E-13.*T.^2;
    A = A0+A1*P+A2*P^2+A3*P^3;
    B = -1.922E-2-4.42E-5.*T+(7.3637E-3+1.7945E-7.*T)*P;
```

```
29      C=-7.9836E-6*P+1.727E-3;
30      c = c0 + c1*P + c2*P^2 +c3*P^3+ A.*S+B.*S.^(3/2)+C.*S.^2;
31
32      % c := sound speed [m/s]
```

C-2 MAV model parameters

The used absorption model has the following empirical parameters.

$$parameters \begin{cases} A_1 = 0.101 * exp((pH - 8)/0.57) \\ P_1 = 1 \\ f_1 = 0.91 * sqrt(S/35) * exp(T/33) \\ A_2 = 0.56 * (S/35) * (1 + T/76) \\ P_2 = exp(-z/4.9) \\ f_2 = 46.6 * exp(T/18) \\ P_3 = 1 - 3.83 * 10^{-2} * z + 4.9 * 10^{-4} * z^2 \end{cases} \tag{C-1}$$

C-3 Attenuation and dispersion

Figure C-1 shows the envelopes (with major signal interpolation of 50 times the sample frequency) for a single type of chirp at different receiver distances. The Figure shows the slight low-pass effect due to the MAV-absorption model.

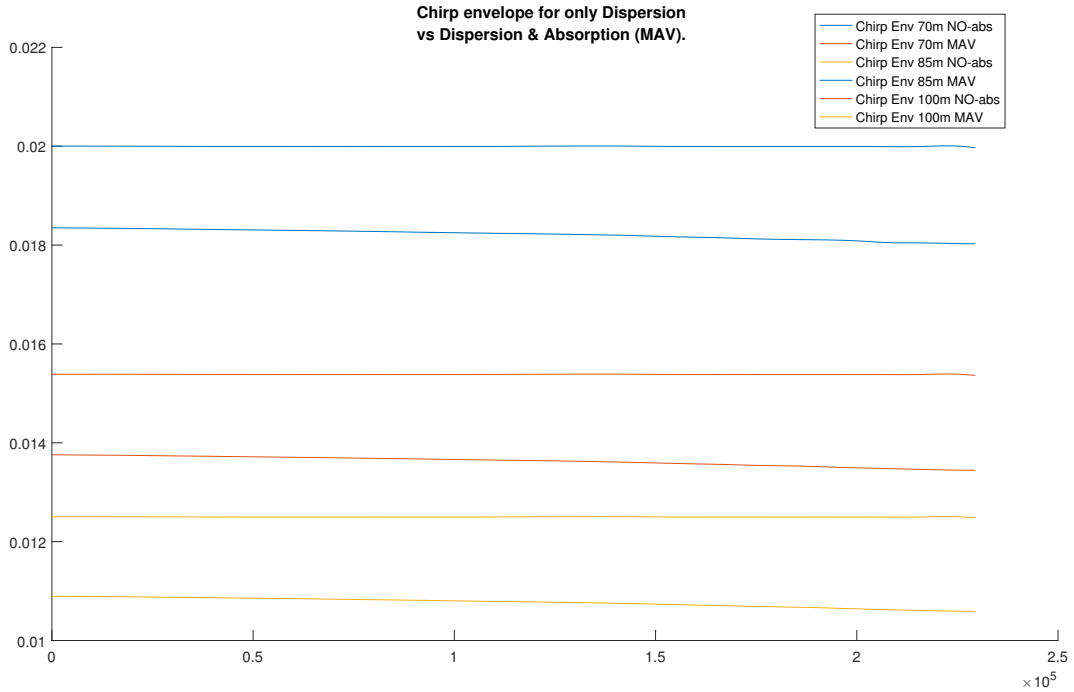

Figure C-1: Chirp envelope through system for different distances. The chirp starts at lower frequency limit and ends at upper frequency limit. Note the slight low-pass-effect for higher frequencies at the end of the chirp.

Appendix D

Reflections

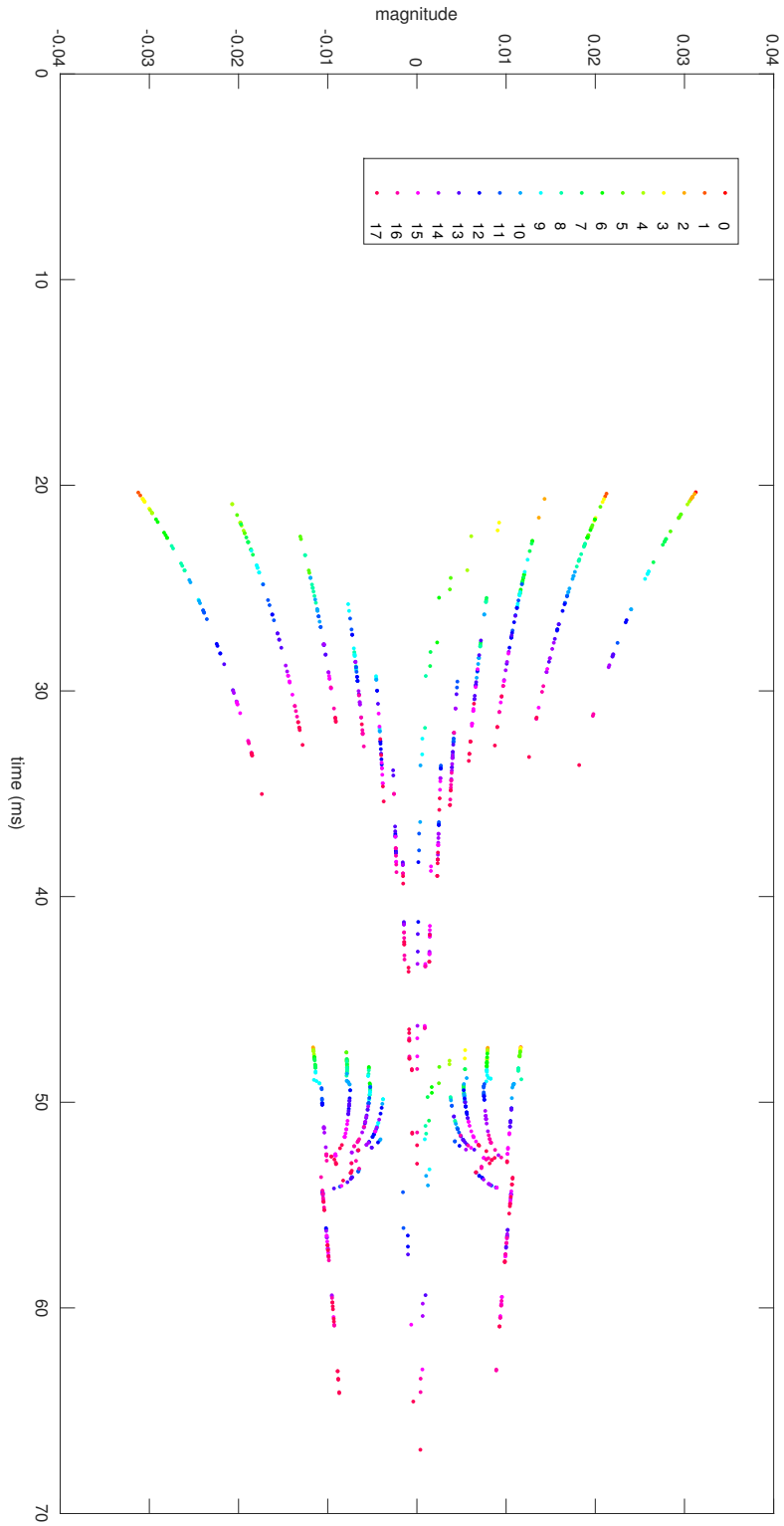

Figure D-1: A colour map of reflections occurring in the channel. The numbers correspond with the reflection order. The receiver was at (x = 20.00m, y =0.50, z =1.85m) and the transmitter at (x=50.00m,y= 3.00m, z=1.85m)

Bibliography

[1] D. Borota, *Design of a position determination system for a ship's hull maintenance robot.* Delft, NL: Faculty of Faculty of Electrical Engineering, Mathematics and Computer Science (EEMCS) Delft University of Technology, July, 2015.

[2] J. Jones and D. Karman, *Modelling the effects of hardware: For devices used in an underwater acoustic positioning system based on channel estimation.* Delft University of Technology, 2016.

[3] C. Kokke and J. Blom, *Validation of models for use in localisation: For a propagation model of an underwater acoustic signal in a shallow-water environment and accompanying hardware models.* Delft University of Technology, 2016.

[4] R. Su *et al.*, *A review of channel modeling techniques for underwater acoustic communications.* IEEE Newfoundland and Labrador Section, 180 Portugal Road, Holiday Inn, St. John's, Newfoundland, Canada, 2010.

[5] P. C. Etter, *Underwater Acoustic Modeling and Simulation.* 11 New Fetter Lane, London EC4P 4 EE: Spon Press, 2003.

[6] R. Alkan, Y. Kalkan, and N. Aykut, "Sound velocity determination with empirical formulas and bar check," in *Proceedings of 23rd FIG Congress, Munich*, 2006.

[7] W. A. Kuperman, "Acoustic propagation modeling in shallow water," *U.S. Navy Journal of Underwater Acoustic*, vol. 51, pp. 275–293, January 2001.

[8] W. A. Kuperman and J. F. Lynch, "Shallow-water acoustics," *Physics Today*, pp. 55–61, October 2004.

[9] X. Lurton, *An introduction to Underwater Acoustics.* Chichester, UK: Praxis Publishing Ltd., 2002.

[10] K. v. Gemeren, J. v. Kampen, J. Poort, and Y. v. Staaden, *Modeling of an underwater acoustic channel in a harbor-like environment.* Delft University of Technology, January 2016.

[11] F. H. Fisher and V. P. Simmons, "Sound absorption in sea water," *The Journal of the Acoustical Society of America*, vol. 62, no. 3, pp. 558–564, 1977.

[12] M. A. Ainslie and J. G. McColm, "A simplified formula for viscous and chemical absorption in sea water," *The Journal of the Acoustical Society of America*, vol. 103, no. 3, pp. 1671–1672, 1998.

[13] C. A. M. van Moll, M. A. Ainslie, and R. van Vossen, "A simple and accurate formula for the absorption of sound in seawater," *IEEE Journal of Oceanic Engineering*, vol. 34, pp. 610–616, Oct 2009.

[14] B. Girod, R. Rabenstein, and A. Stenger, *Signals and Systems*. Baffins Lane, Chichester, West Sussex, PO19 IUD, England: John Wiley & Sons Ltd, 2001.

[15] J. M. Hovem, H. Dong, and X. Li, *Acoustic Sensing Techniques for the Shallow Water Environment: Inversion Methods and Experiments*, ch. A forward model for geoacoustic inversion based on ray tracing and plane-wave reflection coefficients, pp. 241–255. Dordrecht: Springer Netherlands, 2006.

[16] M. Stojanovic, "Underwater acoustic communications: Design considerations on the physical layer," in *Wireless on Demand Network Systems and Services, 2008. WONS 2008. Fifth Annual Conference on*, pp. 1–10, Jan 2008.

[17] P. Qarabaqi and M. Stojanovic, "Statistical modeling of a shallow water acoustic communication channel," in *Proc. Underwater Acoustic Measurements Conference, Nafplion, Greece*, pp. 1341–1350, Citeseer, 2009.

[18] M. Stojanovic and J. Preisig, "Underwater acoustic communication channels: Propagation models and statistical characterization," *IEEE Communications Magazine*, vol. 47, pp. 84–89, January 2009.

[19] S. Sakamoto, H. Tsuru, M. Toyoda, and T. Asakura, *Methods and Applications of Wave-Based Computation*. Springer, Japan, 2014.

[20] Nick Clark, "tinyfdtd." http://www.mathworks.com/matlabcentral/fileexchange/21000-tiny-fdtd-v1-0/content/Tiny_FDTD_v1.m, August 2008.

[21] e. a. Polprasert, Chantri, "Sensor network for acoustic source localization using acoustic fingerprint in urban environments and construction sites," in *Proceedings of the International Symposium on Automation and Robotics in Construction and Mining (Seoul, South Korea)*, pp. 581–587, 2011.

[22] D. Mennitt and M. Johnson, "Multiple-array passive acoustic source localization in urban environments," *The Journal of the Acoustical Society of America*, vol. 127, no. 5, pp. 2932–2942, 2010.

[23] M. P. Maung and H. M. Tun, "Implementation of acoustics based time reversal mirrors for source localization," *International journal of scientific & technology research*, 2014.

[24] W. Sun, G. Videen, Q. Fu, and Y. Hu, "Scattered-field fdtd and pstd algorithms with cpml absorbing boundary conditions for light scattering by aerosols," *Journal of Quantitative Spectroscopy and Radiative Transfer*, vol. 131, pp. 166–174, 2013.

[25] T.-W. Lee and S. C. Hagness, "Pseudospectral time-domain methods for modeling optical wave propagation in second-order nonlinear materials," *JOSA B*, vol. 21, no. 2, pp. 330–342, 2004.

[26] Apache Software Foundation, "openpstd." http://www.openpstd.org/index.html, April 2016.

[27] B. E. Treeby and B. T. Cox, "k-wave: Matlab toolbox for the simulation and reconstruction of photoacoustic wave fields," *Journal of biomedical optics*, vol. 15, no. 2, pp. 021314–021314, 2010.

[28] B. C. Bradley Treeby and J. Jaros, "k-wave." http://www.k-wave.org/documentation.php, November 2012.